Flow-to-Friction Transition in Simulated Calcite Gouge: Experiments and Microphysical Modelling

Jianye Chen[1, 2,*], B. A. Verberne[3], and A. R. Niemeijer[1]

[1] *HPT Laboratory, Department of Earth Sciences, Utrecht University, the Netherlands*

[2] *Faculty of Civil Engineering and Geosciences, Technical University of Delft, Delft, the Netherlands*

[3] *Geological Survey of Japan, National Institute of Advanced Industrial Science and Technology, Tsukuba, Japan*

* Corresponding author: Jianye Chen (e-mail: j.chen3@uu.nl)

Address: Princetonlaan 4, 3584 CB Utrecht, The Netherlands

Key Points:

- We present a transition from flow to friction with increasing slip rate for a simulated carbonate fault sheared at 550 ˚C.
- A microphysically-based model reproduces the lab-observed flow-to-friction transition, including the transient frictional/flow behaviors
- Faults exhibit semi-brittle flow behavior by creep cavitation prior to earthquake rupture at the BDT zone, which serves as precursory phase.

Key words:

Calcite friction, Flow-to-friction transition, brittle-to-ductile transition, microphysical model, earthquake nucleation, rock deformation mechanisms

Abstract

A (micro)physical understanding of the transition from frictional sliding to plastic or viscous flow has long been a challenge for earthquake cycle modelling. We have conducted ring-shear deformation experiments on layers of simulated calcite fault gouge under conditions close to the frictional-to-viscous transition previously established in this material. Constant velocity (v) and v-stepping tests were performed, at 550 ˚C, employing slip rates covering almost six orders of magnitude (0.001 – 300 μm/s). Steady-state sliding transitioned from (strong) v-strengthening, flow-like behavior to v-weakening, frictional behavior, at an apparent 'critical' velocity (v_{cr}) of ~0.1 μm/s. Velocity-stepping tests using $v < v_{cr}$ showed 'semi-brittle' flow behavior, characterized by high stress-sensitivity ('n-value') and a transient response resembling classical frictional deformation. For $v \geq v_{cr}$, gouge deformation is localized in a boundary shear band, while for $v < v_{cr}$, the gouge is well-compacted, displaying a progressively homogeneous structure as the slip rate decreases. Using mechanical data and post-mortem microstructural observations as a basis, we deduced the controlling shear deformation mechanisms, and quantitatively reproduced the steady-state shear strength-velocity profile using an existing micromechanical model. The same model also reproduces the observed transient responses to v-steps within both the flow-like and frictional deformation regimes. We suggest that the flow-to-friction transition strongly relies on fault (micro-)structure and constitutes a net opening of transient micro-porosity with increasing

shear strain rate at $v < v_{cr}$, under normal-stress-dependent or 'semi-brittle' flow conditions. Our findings shed new insights into the microphysics of earthquake rupture nucleation and dynamic propagation in the brittle-to-ductile transition zone.

1. Introduction

Within the seismogenic zone and above, fault displacement is achieved by frictional shear deformation, whereas at much deeper levels in the crust this dominantly occurs by thermally-activated creep mechanisms. Under "fully-plastic", "-ductile", or "-viscous" conditions, creep flow is fast enough to inhibit unstable fault rupture (Scholz, 1988; Meissner & Strehlau, 1982). The transition with increasing depth (or temperature) from frictional fault slip to fully-plastic flow is gradual, involving a competition between time-insensitive (e.g. granular flow) and thermally activated time-sensitive (creep) deformation mechanisms over a depth range of several km's, or a few tens to hundreds of degrees Celsius (e.g., Kawamoto & Shimamoto, 1997; Holdsworth et al. 2001; Imber et al. 2008; Bos & Spiers, 2002; Niemeijer & Spiers, 2006). This depth interval, termed the "frictional-viscous" or "brittle-to-ductile transition" (BDT) zone, is characterized by aseismic as well as seismic fault motion, as implied by field observations of coexisting mylonites and pseudotachylytes (e.g., Stipp et al., 2002; Ueda et al., 2008; Bestmann et al., 2012; Hayman & Lavier, 2014). A comprehensive understanding of the (micro)physical processes leading to fault rupture, is needed to improve numerical models of earthquake fault dynamics within and beyond the BDT (Tse & Rice 1986; Shimamoto & Noda, 2014; Jiang & Lapusta, 2016).

To capture the frictional-viscous or BDT quantitatively and construct or test a constitutive law, a dataset covering a wide range of slip velocities and temperatures is key. Synthetic and natural fault rocks with composite mineralogical compositions (e.g., halite- and quartz-phyllosilicate mixtures) as well as natural fault gouges exhibit transitional shear deformation behavior from frictional slip to viscous flow with decreasing slip rate (e.g., Shimamoto, 1986; Chester & Higgs, 1992; Blanpied et al., 1995; Bos & Spiers, 2002; Noda & Shimamoto, 2010; den Hartog & Spiers, 2013; Niemeijer et al., 2016, 2018). To our knowledge, powdered halite remains thus far the only simulated fault rock for which the complete transition from friction to flow with decreasing slip rate has been demonstrated experimentally (Shimamoto, 1986; Chester, 1988). This is important, because laboratory simulations combined with (post-mortem) microstructural observations enable systematic investigation of the microphysical processes controlling the BDT.

Verberne et al. (2015, 2017) conducted ring shear experiments on layers of simulated calcite fault gouge at temperatures (T) of 20 - 600 ˚C and effective normal stresses (σ_n) up to 120 MPa. At a normal stress, σ_n, of 50 MPa, transitions with increasing temperature were observed from stable (aseismic), v-strengthening to potentially unstable (seismogenic), v-weakening at ~100 ˚C, and back to stable, v-strengthening at ~600 ˚C. The latter transition, from unstable to stable slip at high temperatures, was interpreted to represent a change from frictional deformation in localized, porous slip zones to (more) distributed, dense ductile flow. Existing constitutive models follow an ad-hoc approach, connecting the strength envelops of empirical friction and flow laws (Brace & Kohlstedt, 1980; Reinen et al., 1992; Chester & Higgs, 1992; Beeler, 2009; Shimamoto & Noda, 2014), or else by introducing an empirical T-dependence (Chester, 1994) or an evolution of grain contact area (Aharonov & Scholz, 2018, 2019) to the rate-and-state dependent friction

(RSF) laws. However, a fully microphysically-based constitutive model, calibrated to (post-mortem) microstructural observations, is lacking.

We investigate the mechanical and microstructural characteristics of the frictional-to-viscous (or brittle-to-ductile) transition in simulated calcite gouge, at T = 550 ˚C and σ_n = 50 MPa, using displacement rates spanning 6 orders of magnitude. Our aim was to document, for the first time, the complete flow-to friction-transition with increasing slip velocity in simulated fault rock composed of monomineralic calcite. We employed a microphysically-based constitutive model for shear of gouge-filled faults (the CNS model; Niemeijer & Spiers, 2007; Chen & Spiers, 2016; Chen et al., 2017; Chen & Niemeijer, 2017; Chen et al., 2020) to quantitatively explain the experimentally observed, steady-state and transient friction/ flow behavior. Specifically, we link fault shear strength to internal changes in porosity with increasing displacement, controlled by the competition between intergranular dilatation by granular flow and creep-controlled compaction. Using our experimental and microstructural observations as a basis, combined with microphysical modelling, we discuss implications for fault slip behavior within the BDT zone.

2. Materials and Methods

2.1. Material and Deformation Apparatus

We conducted experiments on simulated fault gouges composed of pure calcite, using the hydrothermal ring shear apparatus installed at Utrecht University (Fig. 1A). Simulated calcite gouge was prepared from crushed, Iceland Spar ($CaCO_3$) single crystals, sieved to a particle size fraction of less than 28 μm (the same as used by Verberne et al., 2015, 2017). X-ray diffraction analysis showed the calcite gouge to consist of 98% calcite, with minor (≤ 2%) dolomite. In each experiment, ~0.65 g of calcite powder was distributed in the annular space between two grooved René-41 Ni-alloy pistons and confined by an outer and an inner ring with a diameter of 28 mm and 22 mm, respectively (Fig. 1B, C). To reduce wall friction, the confining rings were lubricated using Molykote D-321R anti-friction coating. In our experiments we measured shear displacement using a potentiometer attached to the pressure vessel. Displacement normal to the shearing direction (i.e., compaction/dilatation) was measured using a linear variable differential transducer attached to the Instron frame. For more details on the apparatus we refer to Niemeijer et al. (2008, 2016).

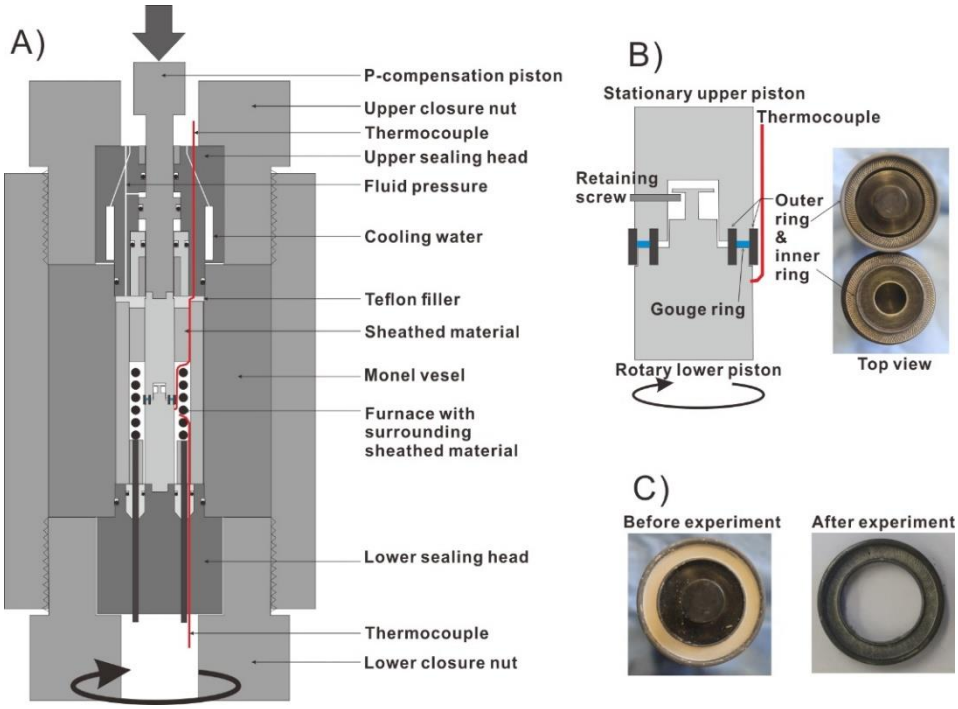

Figure 1. The Utrecht ring-shear hydrothermal pressure vessel and sample assembly used. a) Cross section of the pressure vessel, b) blow up of the sample-piston assembly including the top view of the pair of pistons and confining rings, and c) simulated gouge layers before and after a shear experiment.

2.2. Experimental Conditions, Procedures, and Data analysis

All experiments were conducted at a temperature (T) of 550 ˚C, an effective normal stress (σ_n) of 50 MPa, and a pore fluid pressure (P_f) of 100 MPa (the same T-σ_n-P_f) conditions as used by Verberne et al. (2017). We used a constant sliding velocity (v) ranging between 0.027 μm/s and 300 μm/s, or else we employed sequentially stepped values in the range from 0.001 to 300 μm/s. Our experiments achieved total shear displacements (x) ranging between 5.4 mm and 10.2 mm. The test conducted at v = 0.027 μm/s ran for ~56 hours. Even lower shear displacement rates were achieved by adding an additional gear box to the rotational drive system. This was used in ~3-fold, downward-only v-stepping tests with an initial v of 0.1 μm/s (i.e., v = 0.1 → 0.03 → 0.01 → 0.003 → 0.001 μm/s), except one test using 0.1 → 0.03 μm/s. We imposed downward-only v-steps with the aim to avoid shear strain localization effects in the sample at low strains in the experiment. We also conducted v-stepping tests covering relatively high slip rates, using 3-fold and 1.75-fold steps in the range from 0.1 μm/s to 300 μm/s. Table 1 shows a list of the v-step sequences imposed in each experiment.

Upon terminating an experiment, we first removed the shear stress by rotating the vessel including lower internal piston in the opposite direction, at 1 μm/s, followed by a decrease of the normal stress to ~4.2 MPa (= 1 kN normal load). To prevent vaporization of pore water, we gradually lowered the temperature while simultaneously maintaining the fluid pressure above ~22 MPa (i.e., the supercritical pressure of water, and see a represent annealing curve in the Supplement). Upon reaching T < 100 ˚C, the vessel was depressurized to atmospheric conditions, the remaining normal load was removed, and the piston-sample assembly was disassembled. In total, it took about 45 minutes between termination of the experiment and removal of the sample from the pressure vessel.

In the ring-shear apparatus the confining rings are unsealed, so the fluid present in the pressure chamber (demineralized water) has direct access to the sample, and acts as a pore fluid. The piston-sample assembly is fluid pressure-compensated (Fig. 1A), so that the effective normal stress (σ_n) acting on the sample layer can be calculated directly from the applied normal load, minus a contribution from the O-ring seals (~2.85 MPa). The externally measured torque was corrected for dynamic seal friction using displacement- and pore pressure-dependent calibrations following Den Hartog et al. (2013). The shear stress (τ) supported by the sample was determined assuming a uniform load distribution over the width of the annular sample (3 mm). Standard error propagation analysis showed that $\delta\tau \leq 0.1\%$. Experiments which employed relatively low displacement rates (v < 1 μm/s) spanning relatively long durations (> 20 hours), showed fluctuations in τ resulting from poor temperature control (±3 ˚C worst case). The steady-state shear stress (or shear strength, τ_{ss}) was determined as the average τ-value over a 2 – 4 mm slip interval, with the uncertainty being twice the standard deviation. The friction coefficient (μ) was calculated by dividing the shear stress by the seal friction-corrected σ_n-value, ignoring cohesion of the sample layer (i.e., $\mu = \tau/\sigma_n$).

2.3. Sample Recovery and Microstructural Analysis Methods

For each experiment, recovered sample fragments were impregnated using an epoxy resin, left to harden for several days, and used to prepare polished thin sections in an orientation normal to the shear plane and (sub-)parallel to the shear direction. Each sectioned sample was first analyzed using a Leica polarizing-light microscope, in transmitted light. Selected sections were subsequently investigated using a FEI Helios Nanolab G3, or a Zeiss Sigma-0380 scanning electron microscope (SEM). To enable conduction in the SEM, the sectioned samples were sputter-coated with a ~7 nm thick layer of Pt/Pd. Because our samples are composed almost entirely of calcite, we found that imaging in secondary electron (SE) mode was more effective compared with backscattered electron (BSE) mode. Imaging was achieved with an acceleration voltage of 5 to 10 kV and a beam current of 0.2 to 1.6 nA. Selected SE micrographs were analyzed using the linear intercept method to obtain the grain size (d) distribution, assuming $d = 1.5L$ where L is the measured apparent grain diameter as observed in our sectioned samples (following Gifkins, 1970).

To investigate the crystallographic orientation distribution of the calcite grains after shear deformation we conducted electron backscatter diffraction (EBSD) analysis, using an Oxford Instruments (OI) EBSD detector mounted on the Zeiss Sigma-0380 SEM. Prior to EBSD measurements we re-polished the sections with a silica colloid, followed by coating with a carbon film of less than 4.0 nm thickness. Automated EBSD mapping of rectangular areas ~25 μm × 25 μm to 1 mm × 0.5 mm in size was carried out employing an accelerating voltage of 15 to 20 kV, beam current of ~2 nA, an aperture of 50 μm, a working distance of ~20 mm, and a step size ranging from 0.35 to 2.0 μm depending on the (average) grain size of the mapped area. The Kikuchi band pattern at each measurement or pixel was automatically indexed using OI AZtec software. Indexing in maps of the bulk sample was relatively successful (indexing success rate (ISR) of 50 – 88%). However, within shear bands, indexing was relatively poor (ISR < 20 %), even for the lowest step-size employed. For each EBSD map we carried out repeat measurements in 2 or 3 corresponding areas of the sample. Crystallographic orientation data are plotted in upper hemisphere, equal area, stereographic projections, with contours of mean uniform density (MUD)

generated using a half width of 15° and cluster size of 5°.

3. Results

3.1. Mechanical Data

We plot the shear stress τ (or friction coefficient μ) versus shear displacement x in Figure 2. All experiments and key parameters are listed in Table 1. For each experiment conducted using $v >$ 0.1 μm/s the curves show rapid, near-linear loading in the first ~0.5 mm of shear displacement, a well-defined peak friction value of ~1.0 at $x \approx$ 0.5-1.1 mm, followed by rapid, near-exponential decay to a steady-state friction value achieved after $x \approx$ 4-5 mm (Fig. 2A). By contrast, for experiments using $v \leq$ 0.1 μm/s, initial, near-linear loading was followed by apparent 'yield', gradual hardening to a maximum friction value, and either gradual weakening or else steady-state sliding at a near-constant shear strength value (Fig. 2B).

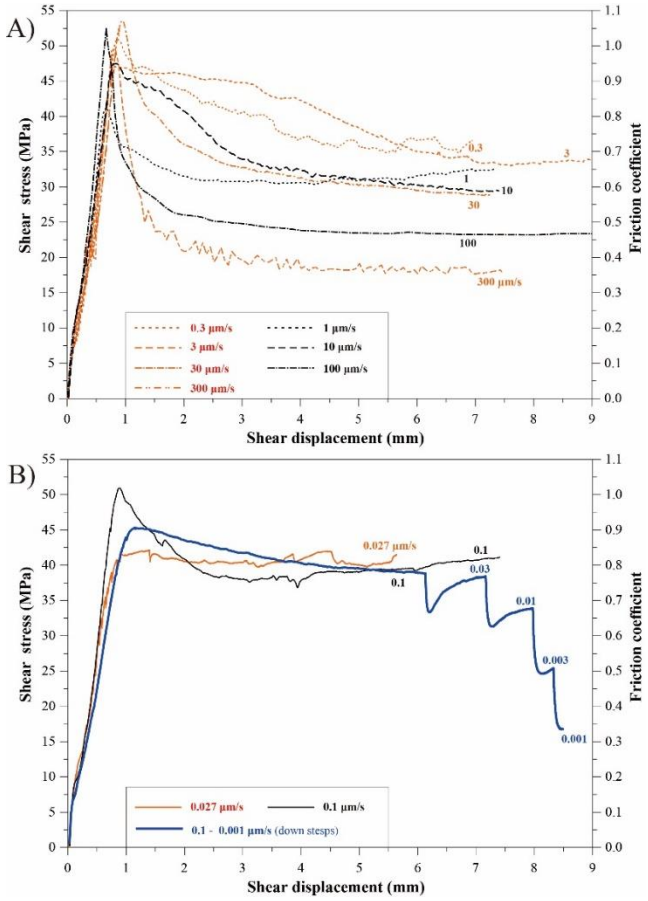

Figure 2. Rotary shear experiments on layers of simulated calcite fault gouge conducted at 550 ˚C, 100 MPa fluid pressure, and 50 MPa effective normal stress conditions. The tests were run at constant velocities (v) falling in the range from 0.027 to 300 μm/s. Result from a downward v-step experiment was added (in thick blue line), giving the steady states for v from 0.1 μm/s to 0.001 μm/s. For better illustration, the results were only plotted to a shear displacement of 9.0 mm, and the data were separated into a) with $v >$ 0.1 μm/s and b) with $v \leq$ 0.1 μm/s.

For the v-stepping experiment conducted using $v \leq$ 0.1 μm/s (u605), the strength values observed at the peak and at steady-state during initial sliding at v = 0.1 μm/s, are broadly

consistent with those observed in the constant-v experiment (u516, Fig. 2b). Downward steps in v consistently triggered a sharp drop in shear resistance, followed by gradual re-strengthening to a markedly lower, steady-state strength value (Fig. 2b), implying strong v-strengthening behavior. In the upward v-stepping tests conducted using $v \geq 1.0$ μm/s, each individual step showed 'classical' rate-and-state-friction (RSF) behavior, that is, a direct increase in μ-value followed by an exponential decay to a new steady state μ_{ss} (Fig. 3; for background on RSF theory see e.g., Marone, 1998). For all the v-steps investigated, μ_{ss} consistently showed negative rate dependence (i.e., $d(\Delta\mu_{ss})/d(\ln v) < 0$), or v-weakening behavior. The 'peak' direct effect, in RSF known as the 'a'-value, decreases with increasing v (Figs. 3A, B). At lower velocities, the slip distance required to re-attain steady-state sliding ('D_c' in RSF) is observed to increase, with the v-steps at low displacements not reaching steady state within ~0.5 mm slip interval. During the interval at v = 100 μm/s (experiment u502), sudden, drastic weakening occurred, followed by an extraordinarily large direct effect when stepping to 300 μm/s (Fig. 3A). Similar drastic weakening at v = 100 μm/s was also reported by Verberne et al. (2015).

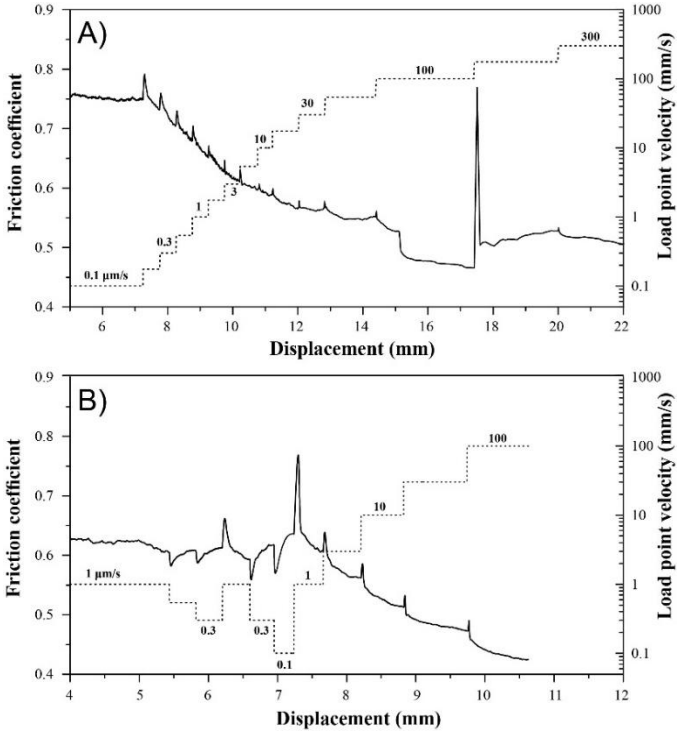

Figure 3. Results from two velocity-stepping tests in the high velocity range (0.1 – 100 μm/s). The experimental conditions are the same as that in Figure 2.

Mean values of the steady-state shear strength (τ_{ss}) or μ_{ss} (= τ_{ss}/σ_n) from the constant-v and the v-stepping experiments are plotted against log(v) in Figure 4. In both types of experiments, the uncertainty in the shear strength measurements ($\Delta\tau_r$, indicated by the error bars in Fig. 4) is less than ±1.3 MPa, except for the data obtained at v = 100 μm/s in v-stepping test u502 for which $\Delta\tau_r$ = ± 2.3 MPa. In general, data from all experiments are consistent, pointing to a transition with increasing v in the sign of $d\mu_{ss}/d\log(v)$, from positive to negative, around a 'critical' velocity (v_{cr}) of ~0.1 μm/s.

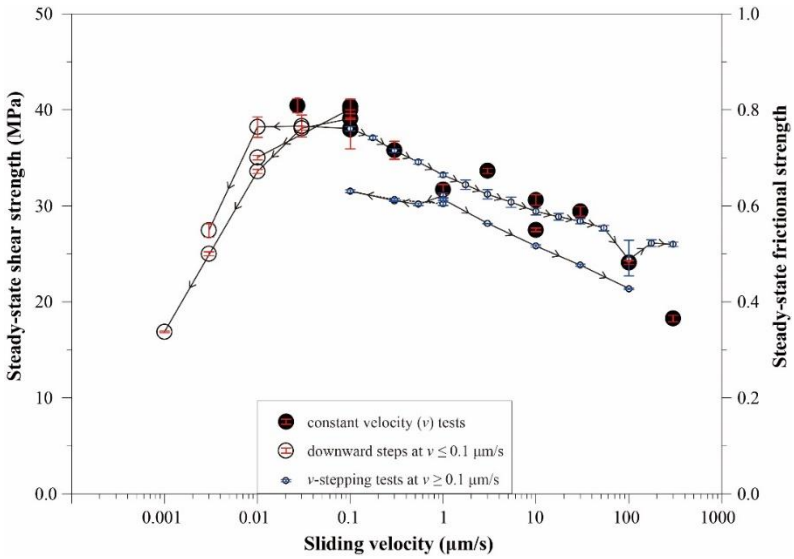

Figure 4. Steady-state shear strength as a function of sliding velocity for a simulated calcite fault gouge sheared at 550 ˚C and 50 MPa effective normal stress conditions. Data are derived from the experiments shown in Figures 2 and 3, and another two from Verberne et al., (2017) (see Table 1 for details). The red bars give the errors to steady-state shear strength for individual velocity steps.

3.2. Microstructures

Upon sample recovery after an experiment we found that samples that were sheared at low v ($\leq$ 0.1 μm/s) could be extracted as a single, coherent piece, whereas samples sheared at high v (> 0.1 μm/s) typically broke along shear plane-parallel and inclined shear fractures, resulting in multiple arc-shaped fragments. Transmitted light micrographs of sections prepared from each experiment are shown in Supplementary Figure S1. Below we describe the microstructures of representative samples u605, u508, and u635, which were deformed using final displacement rates in the experiment (v_{final}) of respectively 0.001 μm/s, 0.03 μm/s, and 10 μm/s (see Table 1).

3.2.1. Light and Electron Microscope Observations

Sample u605 (v_{final} = 0.001 μm/s) showed a dense, near-uniform microstructure composed of apparently rounded grains as observed under plane polarized light (PPL) (Fig. 5A, see also Fig. S1). We observed no evidence for localization of shear deformation. Secondary electron (SE) micrographs revealed that the sample is characterized by densely-packed polygonal grains, frequently with ~120˚ triple junctions (Fig. 5A). Occasionally, the grains are elongated, with a long axis oriented (sub-) parallel to the shear plane (Fig. 5A). The grain size distribution (GSD) has a range of d = 1.0 - ~7.0 μm (N = 363), and a mean ($\bar{d}$) of ~3 μm. Sample u508 (v_{final} = v = 0.03 μm/s) showed light- and dark-grey bands oriented parallel and inclined to the shear plane and -direction, as observed using PPL (Fig. 5B). We infer that these bands are an artifact from section preparation, possibly representing different degrees of epoxy impregnation. SE micrographs show that this sample has an overall dense microstructure with widespread polygonal grains, resembling the microstructure of sample u605 which was sheared at v_{final} = 0.001 μm/s (cf. Fig. 5A). The GSD (N = 420) has a range d = 1 to 14 μm and $\bar{d}$ = 4 μm.

Microstructures of samples that were sheared using v_{final} > 1.0 μm/s consistently showed the presence of a ~20 to 60 μm wide, shear-plane parallel zone composed of ultra-finely comminuted

grains, located along at least one of the sample boundaries. For most samples, this boundary (B) shear band was only partially recovered. Light microscope observations of sample u635 (v_{final} = v = 10 μm/s), under crossed-polarized light (XPL) using the gypsum plate inserted, revealed that the B-shear is characterized by a strong uniform birefringence and optical extinction, suggestive of a crystallographic preferred orientation (CPO) (Fig. 5C). Using a light microscope grains within the B-shear cannot be resolved, whereas in the adjacent bulk gouge, the grains are angular, randomly packed, and have a size-range close to that of the starting material (d = 0.7 - 50 μm, with $\bar{d}$ = 20 μm, Fig. 5C-1). SE micrographs revealed that the B-shear is relatively porous for most portions (~3-7%), and that the grains are polygonal to rounded with d in the range from 0.3 to 1.5 μm, and $\bar{d}$ = 0.8 μm (cf. Fig 5C-3 and 5A-3).

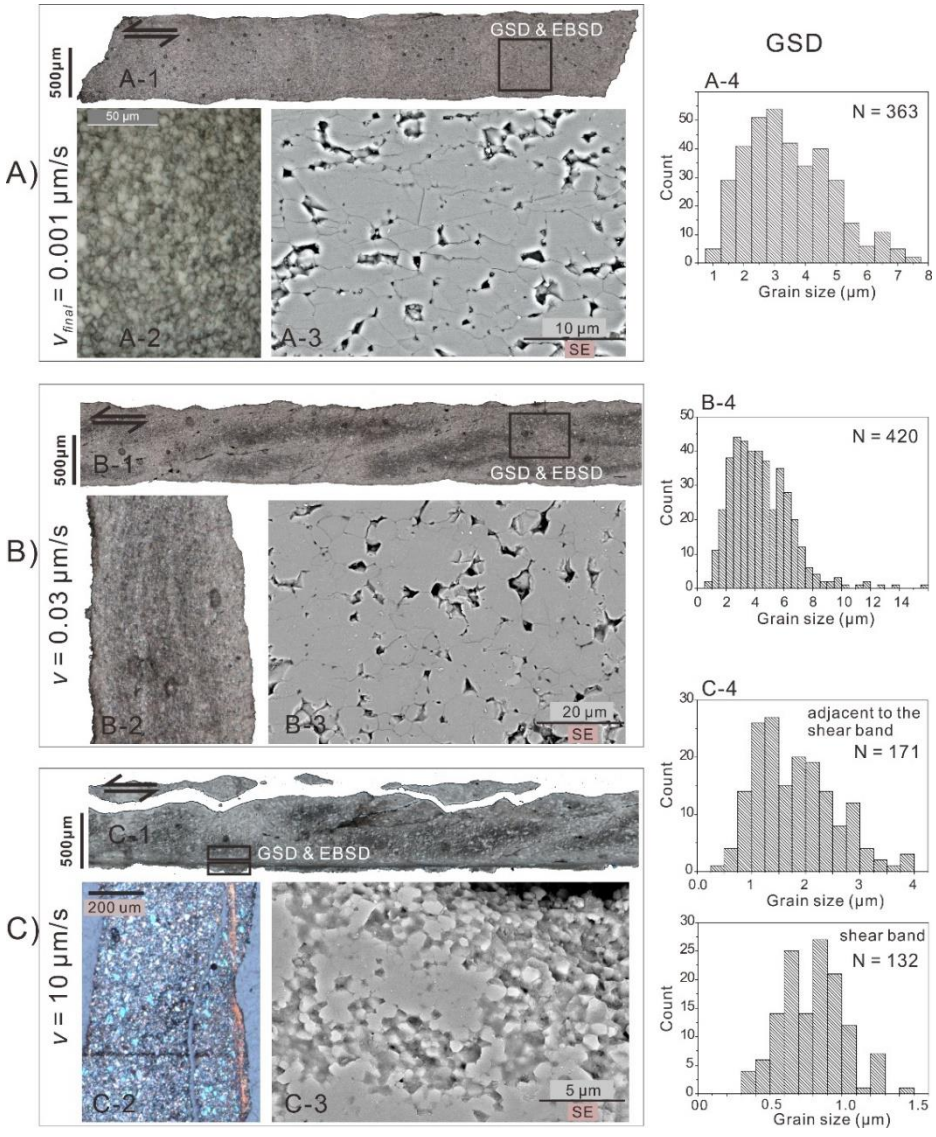

Figure 5. Microstructure of layers of simulated calcite fault gouges from three experiments, sheared at A) v_{final} = 0.001 μm/s (u605), B) constant-v = 0.03 μm/s (u608), and C) constant-v = 10 μm/s (u635), respectively. Each sample is displayed in four panels: (panels A-1, B-1, and C-1), a transmitted light photomosaic of thin section over the entire gouge layer thickness; (panels A-2, B-2, and C-2), an exaggerated area of potential interests; (panels A-3, B-3 and C-3), a SEM image of a representative area or the shear band if present; and (panels A-4, B-4, C-4), a histogram of grain size distribution for

the selected area. Note that the image shown in Panel C2 was taken using cross polarized light with the gypsum plate inserted. For each sample, imaged-based grain size distribution analysis was performed on selected area as marked in rectangles in panels A-1, B-1 and C-1. For the sample sheared at 10 μm/s, these analyses were performed in both the shear band and the adjacent area.

3.2.2. Electron Backscatter Diffraction Analyses

EBSD mapping was carried out of samples u605, u508, and u635, which were deformed at respectively v_{final} = 0.001 μm/s, 0.03 μm/s and 10 μm/s (see Table 1). All maps recorded in 'slow' experiments u605 and u508 (v < 0.1 μm/s) showed ISR ≥ 70% (Figs. 6A, B and see results from more areas in Figs. S2A, B). By contrast, for maps prepared from sample u635, ISR ≤ 61%, with the lowest value of ~20% for a map of a B-shear band (Fig. 6D and Fig. S2D). Stereographic projections revealed strong c-axis maxima in sample u605 (v_{final} = 0.001 μm/s, Fig. 6A), and in the bulk part of sample u635 (v_{final} = v = 10 μm/s, Fig. 6C), but less so in sample u508 (v_{final} = v = 0.03 μm/s). For the shear band in sample u635, as evident from the Euler map in Figure 6D, the data are mostly from a few, relatively large grains. Due to poor indexing (ISR ≤ 20%) it remains difficult to compare these and other data obtained from B-shear bands with other samples.

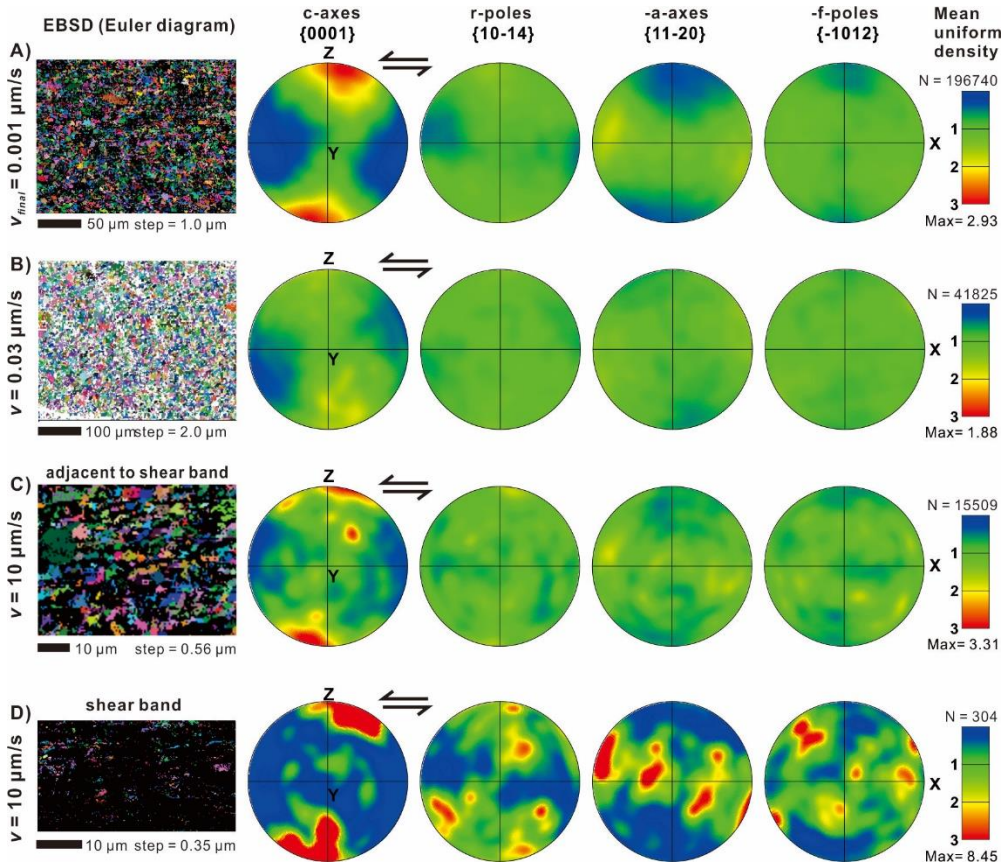

Figure 6. Electron backscatter diffraction (EBSD) of simulated calcite fault gouges retrieved from three experiments, sheared at A) v_{final} = 0.001 μm/s (u605), B) constant-v = 0.03 μm/s (u608), and C), D) constant-v = 10 μm/s (u635), respectively (see the mapped areas in Fig. 5). For sample u635, the analyses were performed in both the shear band and the adjacent area. The left panels give the Euler angle diagram of the mapping area. A step size of 1.0 or 2.0 μm was used in the mapping except for the shear band of u635, where a step size of 0.3 – 0.6 μm was taken. The EBSD data were plotted in upper

hemisphere, equal area pole diagrams for X, Y and Z directions, respectively.

4. Data Analysis and Deformation Mechanisms

4.1. Mechanisms Controlling Shear Deformation at v < 0.1 μm/s

In view of the high temperature (550 ˚C) used in our experiments and the mechanical and microstructural observations reported above, it is reasonable to suppose that creep processes played at least some role in our experiments, especially at the low displacement rates (v < 0.1 μm/s). To investigate this, and to identify a suitable constitutive equation that can be used to model our results, we compare the stress sensitivity of the ductile strain rate (the so-called "n-value") as derived from our low-v shear experiments with values determined from compression experiments on dense calcite polycrystals.

To this end, we first converted the steady-state shear stress (τ) and shear strain rate ($\dot{\gamma}$) in our experiments to an equivalent compressive flow (differential) stress (σ) and strain rate ($\dot{\varepsilon}$), using $\dot{\varepsilon} = \sqrt{3}\dot{\gamma}$ and $\sigma = \sqrt{3}\tau$ (Schmid et al., 1987). The 'slowest' experiments (u605, using v_{final} = 0.001 μm/s) showed a near-homogenously deformed microstructure (Figs. 5A). Taking a uniform shear zone width l of 0.8 mm, this implies that, in experiments using $v_{final} \leq 0.03$ μm/s, $\dot{\gamma} \approx 1.25\times10^{-6}$ to 3.75×10^{-5} $s^{-1}$and $\dot{\varepsilon} \approx 2.17\times10^{-6}$ to 6.50×10^{-5} s^{-1}. For each v-step interval in the experiment, we calculated $\dot{\gamma}$ and $\dot{\varepsilon}$, assuming constant thickness W = 0.8 mm (Fig. 7). A generalized power law stress dependency of the compressive strain rate (i.e., $\dot{\varepsilon} \propto \sigma^n$) implies $n = \mathrm{dlog}(\dot{\varepsilon})/\mathrm{dlog}(\sigma)$, hence an estimate of the n-value can be obtained by taking the slope of the interpolated curve shown in Fig. 7. For each step, the corresponding n-value progressively decreases. Ignoring the first step, all values fall in the range from $n \approx 2.5$ to 8.8, with mean $\bar{n} \approx 3.91$, which falls between n-values reported for flow of dense calcite polycrystals by diffusion creep (1.1 < n < 1.7) and by dislocation creep (4.2 < n < 7.6) (see Table 2, see De Bresser et al. 2002 and references therein). The best match is with the n-value of 3.33 reported by Walker et al. (1990), who best-fit a composite, grain size- and stress-dependent flow law to data from compression experiments on synthetic, hot-pressed calcite aggregates conducted at σ < 25 MPa and T = 400 - 700 ˚C. These authors suggested that grain size-sensitive (diffusion) and -insensitive (dislocation) creep occurred simultaneously in their experiments.

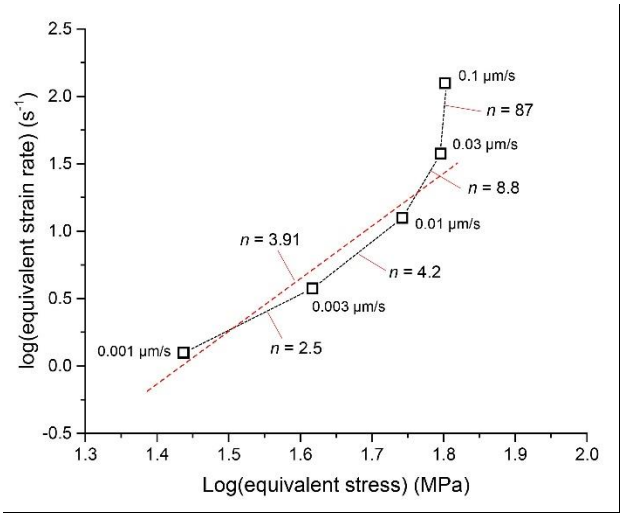

Figure 7. Equivalent strain rate ($\dot{\varepsilon}$) versus equivalent stress (σ) in the logarithmic scale from the

experiment (u605), which was sheared with downward *v*-step sequence from 0.1 μm to 0.001 μm. Assuming a general creep law of a power law form ($\dot{\varepsilon} \propto \sigma^n$), the *n*-value can be obtained using the relation $n = dlog(\dot{\varepsilon})/dlog(\sigma)$ for all the steps, as indicated by the slopes.

Based on the above, we posit that shear deformation at v < 0.1 μm/s in our experiments occurred by a combination of diffusion and dislocation creep processes. Importantly, the operation of dislocation and diffusion creep is consistent with microstructural observations. Firstly, samples sheared at v < 0.1 μm/s showed distributed shear deformation, a relatively low porosity (< ~2%), and polygonal grains characterized by straight grain boundaries and high-angle triple junctions (Figs. 5A-3, 5B-3). The latter are consistent with microstructures formed in compression experiments on dense calcite polycrystals, which deformed by grain size sensitive creep (Schmid et al., 1977; Walker et al., 1990). Furthermore, the presence of 4-9 μm-sized elongated grains in sample u605 (v_{final} = 0.001 μm/s; Fig. 5A) and the c-axis maximum (Fig. 6A, C) are suggestive of intracrystalline plasticity (cf., Walker et al., 1990; Lafrance et al., 1994; Schmid et al., 1987; Rutter et al., 1994). Lastly, the grain size distribution measured in samples sheared at v_{final} < 0.1 μm/s is much narrower than compared with that in the starting material (ranging 1–9 vs 0.7–50 μm), implying that dynamic and or static recrystallization played a role in our experiment (Drury et al. 1985). A simple calculation using the equation given by Covey-Crump (1997) for fluid-assisted grain growth in dense calcite aggregates with d < 10 μm, indicates that, in our 'slow' experiments using $v \leq$ 0.1 μm/s, grain growth is only expected in the first few hours (< 10^4 s) of the experiments. Therefore, this process did not affect our steady-state data.

Combining all of the above, our interpretation is that shear strain accommodation at v < 0.1 μm/s in our experiments occurred by a combination of diffusion and dislocation creep (hereafter referred to the flow regime). However, around the critical velocity v_{cr}, shear strain accommodation is characterized by a 'brittle' component, as indicated by the large stress exponent (n ~ 87) for v = 0.03 - 0.1 μm /s (Fig. 4; Brantut et al., 2013; Chen et al., 2020), and by the 'friction-like' transient response to a step in v (Fig. 2B; Noda & Shimamoto, 2010; Chester, 1988).

4.2. Mechanisms Controlling Shear Deformation at v > 0.1 μm/s

All experiments which explored v > 1.0 μm/s showed v-weakening behavior (Fig. 4). As mentioned above, in these 'fast' experiments the transient response strongly resembled "classical" RSF behavior, and recovered sample fragments consistently showed evidence for shear strain localization in a narrow (20 - 60 μm), boundary-parallel (B) shear band (Fig. 5C, S1). The presence of a B-shear suggests that this accommodated the bulk of the imposed shear deformation (Takahashi et al., 2017; Verberne et al., 2017). Assuming a constant, average shear band thickness of ~40 μm, the internal shear strain rate measured ~2.5×10^{-2} s^{-1} to 6 s^{-1} for v = 1 - 300 μm/s, which is ~6 orders of magnitude higher than that in experiments conducted using $v \leq$ 0.1 μm/s.

The shear band consists of polygonal or rounded grains, resembling the grain cavitated arrays reported to have formed by Verberne et al 2017 in experiments conducted under similar T-σ_n-P_f conditions (Fig. 5C). This, combined with the relatively high shear strain rates acting within the shear bands, implies that granular flow must have played a role. However, plastic creep mechanisms likely also played some role. In view of the high temperatures in our fluid-saturated experiments (550 ˚C), and small mean grain size in the B-shear bands compared with samples sheared at v < 0.1 μm/s, water-assisted diffusion creep ($\dot{\varepsilon} \propto d^{-3}$) is an obvious candidate. On the

other hand, the presence of a CPO, as evident from uniform optical birefringence under a light microscope (Fig. 5C-2), is suggestive of dislocation creep. A c-axis maximum, similar to the one observed in the low-v experiments, was identified in grains adjacent to a B-shear (Fig. 6C and S2), consistent with that reported by Verberne et al. (2017) for internal shear band grains.

Combining all of the above, our interpretation is that in the flow regime (v < 0.1 μm/s) a combination of diffusion and dislocation creep played the dominant role, while at high slip rates (v > 0.1 μm/s, hereafter referred to as the friction regime) granular flow played an important role alongside plastic creep process.

5. Microphysical Modelling

In this section, we use a previously developed microphysical model for shear of granular media, the Chen-Niemeijer-Spiers (CNS) model, to simulate the mechanical behavior of calcite gouge observed in our experiments. The CNS model is capable of quantitatively reproducing steady-state and transient shear behavior, using physics-based input parameters derived from laboratory observations. Constitutive equations of the CNS model are given in the Supporting Information; for details on model development and implementation we refer to Niemeijer & Spiers (2007), Chen & Spiers (2016), Chen & Niemeijer (2017), and Chen et al. (2017).

5.1. Model Framework and Parameters Used

In section 4 we showed that, within the range of sliding velocities corresponding with the frictional regime (v > 0.1 μm/s) in our experiments, shear plane-parallel deformation of a gouge layer of thickness W occurs by the simultaneous operation of granular flow ($\dot{\gamma}_{gr}$) and intergranular plastic creep ($\dot{\gamma}_{pl}$). In the assumed model geometry, granular flow operates in a shear band of width W_{sb}, while intergranular creep may occur involving the entire gouge, including the shear band as well as the adjacent bulk layer (W_{bulk}) (see the Supplementary Information). The implication is that

$$v = W_{sb}\dot{\gamma}_{gr} + W_{sb}\dot{\gamma}_{pl}^{sb} + W_{bulk}\dot{\gamma}_{pl}^{bulk} \quad (1)$$

where W_{sb} + W_{bulk} = W and $\dot{\gamma}_{pl}^{sb}$ and $\dot{\gamma}_{pl}^{bulk}$ are the creep strain rates within respectively the shear band and the bulk layer, in the shear direction. For v < 0.1 μm/s, shear deformation is more homogeneous, hence $W \approx W_{sb}$ and $v = W\dot{\gamma}_{gr} + W\dot{\gamma}_{pl}$.

All parameters and values used in our simulations are listed in Table 3. The temperature and effective normal stress used followed the experimental conditions employed (i.e., T = 550 ˚C, σ_n = 50 MPa). Layer thicknesses (W), grain size (d), and porosities (φ) were set in accordance with post-mortem microstructural observations, where relevant of the shear band and the bulk sample layer. To simulate flow behavior at low velocities (v < 0.1 μm/s), we assumed a homogeneous shear zone of W = 800 μm, with $d \approx 2 - 3$ μm. Conversely, at high velocities (v > 0.1 μm/s), we assumed $W_{sb} \approx 20 - 100$ μm, W_{bulk} = 800 – W_{sb} [μm], and a grain size of respectively 0.8 μm and 5.0 μm. To match the overall shear strength level observed in our experiments (Fig. 4), we assumed a reference grain boundary friction value $\tilde{\mu}^*$ of 0.43 at v = 0.1 μm/s, and a rate dependent coefficient ($a_{\tilde{\mu}}$) of 0.01 (Chen & Spiers, 2016). Porosity and shear stress need to be solved. For both zones we assumed a critical porosity φ_c of 40% (see Vermeer & De Borst, 1984) and a non-zero limit porosity φ_0 of 2% (see the Supplement Text S1 for details).

We used a flow stress- (σ-) and grain size- (d-) sensitive constitutive law to quantify the creep strain rate ($\dot{\varepsilon}$), as calibrated to data from compression tests on dense calcite polycrystals by Walker

et al. (1990) (see Table 2):

$$\dot{\varepsilon} = Aexp\left(-\frac{E_a}{RT}\right)\frac{\sigma^n}{d^m}. \quad (2)$$

Here A is a pre-exponential constant (log$A$ = 6.68 $s^{-1}\mu m^{-m}MPa^{-n}$), E_a is the activation energy (190 $kJmol^{-1}$), T is the temperature, R is the gas constant (8.31 $Jmol^{-1}K^{-1}$), and m = 1.33 and n = 3.33 are empirical constants. In the CNS model we used this creep law for both normal and shear deformation, with slightly different pre-exponential constants ($A_n = A$ and $A_t = \sqrt{3}^{n+1}A$, where A_n and A_t are the constants for normal and shear components, respectively; see Text S1 for detailed description). A porosity function is used to account for changing porosity in the frictional regime (Niemeijer & Spiers, 2007).

To simulate transient behavior, the sheared gouge layer is modeled analogous to a spring-slider system, composed of a linear spring of stiffness K that is activated at a load point at velocity v_{imp}, assuming no inertia;

$$\dot{\tau} = K(v_{imp} - v) \quad (3)$$

The constitutive equations of the CNS model (eq. S1-S5), together with the creep law (eq. 2) and kinematic equations for fault deformation (eq. 1 and 3), can be rewritten into a pair of ordinary differential equations (ODEs) that specify the rate of change of shear stress ($\dot{\tau}$) and porosity ($\dot{\varphi}$). All ODEs are solved using the finite element package COMSOL.

5.2. Simulation Results and Comparison with Experiments

5.2.1. Steady-state Behavior

The CNS model output simulating the steady-state shear strength and porosity change with increasing displacement in our experiments is shown in Fig. 8 and S4. We also carried out sensitivity analysis for grain size and shear band thickness. For a homogeneously shearing gouge layer at $v \leq 0.03$ μm/s, the model predicts strong v-strengthening behavior (Fig. 8A), reaching a 'background' (or limit) porosity φ_0 (Fig. 8B). When plotted in log-log space (Fig. 8A-inset), the τ-v curves are straight lines with dlog(v)/dlog(τ) = n = 3.3 (see eq. 2). As v increases the steady-state porosity begins to increase from the background value, at the dilatation velocity v_{dil} = ~0.03 μm/s (Fig. 8). This onset of dilatation, or, $\varphi(v) > \varphi_0$, is associated with a deviation of the τ-v curve from linearity (Fig. 8A-inset), implying a higher stress sensitivity (or larger 'apparent' n-value). For $v > v_{cr}$ = 0.1 μm/s, constituting localized shear, the model predicts persistent v-weakening and an increasing steady-state porosity with increasing v, with slopes that decrease with increasing v (Fig. 8). For each shear deformation regime ($v < v_{cr}$ and $v > v_{cr}$), the model outcome is generally consistent with the τ-v profile observed in the experiments (Fig. 8 cf. Fig. 4; see a detailed comparison in Fig. S4).

Regardless of the grain size or shear band width used, the τ-v curves show a smooth connection between both shear deformation regimes, that is, within a peak shear stress and velocity window of 38 to 40 MPa and 0.1 to 0.25 μm/s (Fig. 8). However, there is a relatively large offset in porosity, which is unsurprising since the model assumes a different internal fault structure or geometry for the flow ($v < v_{cr}$) vs. the frictional ($v > v_{cr}$) regimes. The microphysical processes controlling the change from distributed to localized slip, at $v \sim v_{cr}$, is not captured by the present model. We note, however, that in the case that there would be no microstructural change at $v = v_{cr}$, the model predicts a continuous transition with increasing slip rate from v-strengthening to

v-weakening behavior (Fig. S5). This suggests that a flow-to-friction transition with increasing slip rate will always emerge from the model and that the microstructure controls the velocity at which the transition from *v*-strengthening to -weakening occurs (i.e., the value of v_{cr}).

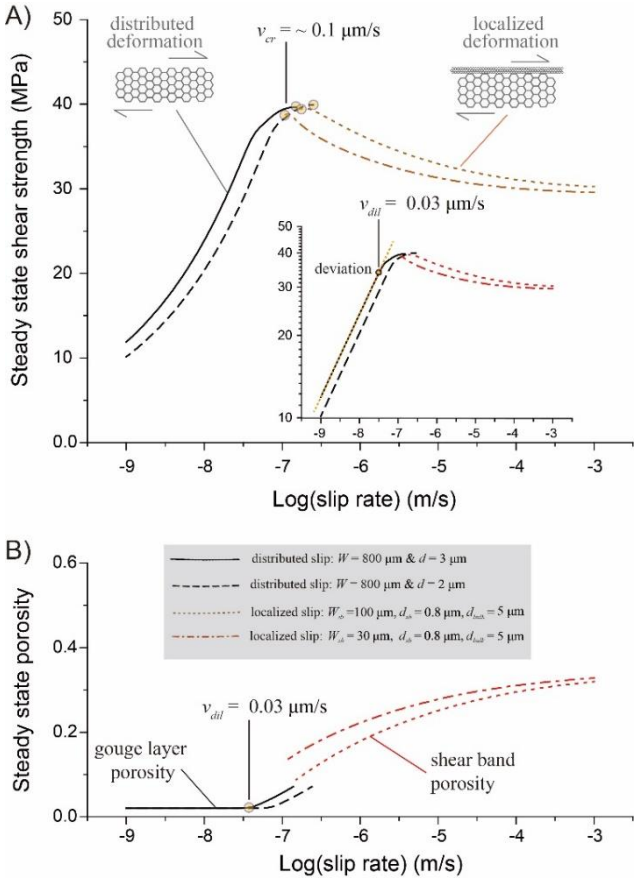

Figure 8. Steady-state A) shear strength and B) porosity as a function of slip velocity for a simulated calcite gouge layer at 550 ˚C and 50 MPa effective normal stress, predicted by the CNS model. The model conditions were set according to the experiments, with different model geometries resembling the microstructures observed at different slip rates. Specifically, for slow slip rates a uniform gouge layer was assumed, while at high slip rates, we assumed localized slip, with different grain sizes and thicknesses for the shear band and the bulk layer. The predicted results indicate in transition from flow to friction at a critical velocity (v_{cr}) of 0.1 μm, consistent with the observation. The inset graph of A) shows the same results but in the log-log scale, where the deviation from a linear line occurs at a velocity corresponding to the onset of dilatation (v_{dil}).

Additional sensitivity analyses, specifically on the effect of varying σ_n, *T*, *d* or d_{sb}, W_{sb} and W_{bulk}, and φ_c and φ_0 (see Table 3 and Supplementary Text for their definition), consistently showed a τ-*v* curve characterized by a continuous transition from strong *v*-strengthening to -weakening behavior (Fig. 9). The critical velocity v_{cr}, which demarcates the transition in the sign of *v*-dependence, ranges from 0.1 to 0.7 micron/s within the range of parameter values tested. Specifically, an increase in (effective) normal stress (σ_n) results in a higher shear strength and an increase in v_{cr}. Increasing the temperature or decreasing the grain size (either *d* or d_{sb}) causes a

rightward horizontal translation of the τ-v curve implying a higher v_{cr}-value. Note that due to the limited thickness of the bulk gouge layer, the grain size (d_{bulk}) has a negligible effect on the shear strength. Lowering φ_c or increasing φ_0 does not change the τ-v profile but leads to a higher peak strength and more pronounced v-weakening in the frictional regime (i.e., for $v > v_{cr}$).

As already shown in Fig. 8, a decrease in W_{sb} causes a leftward horizontal translation of the τ-v curve (see also Fig. S5). Here we further investigated the effect of progressive localization, which may have occurred in the fictional regime at $v > v_{cr}$ that showed v-weakening (Beeler et al., 1996). To mimic this, we assumed a log-linear decrease in W_{sb} from 200 to 10 μm as v increases from the calculated v_{cr} to 1 mm/s. The predicted τ-v curve displays a higher v_{cr} and a deeper v-weakening at $v > v_c$ (Fig. 9D). This may explain why our reference simulation using a constant W_{sb} predicts a gentler v-weakening than observed in the experiment (see the comparison in Fig. S4).

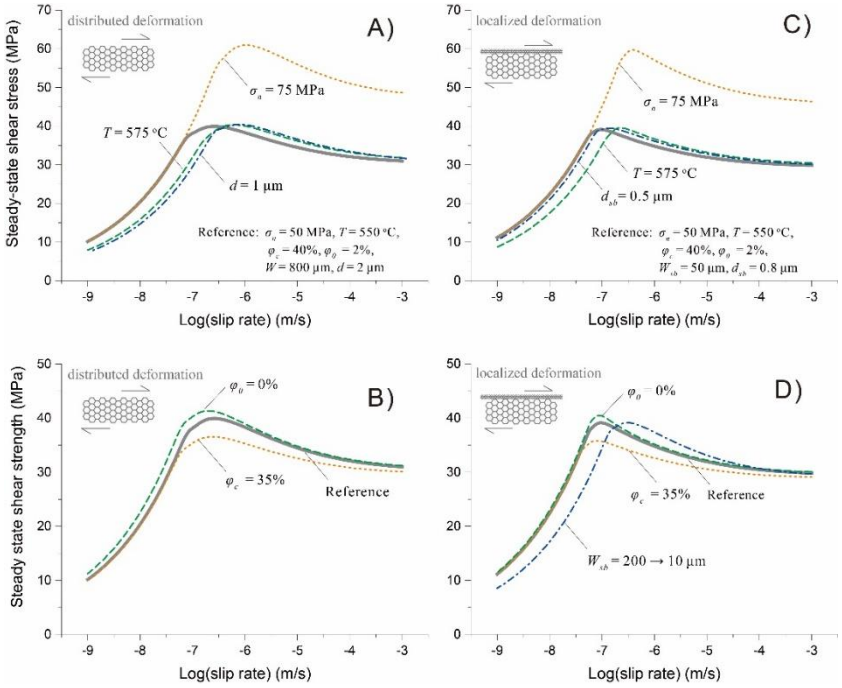

Figure 9. Sensitivity of computed steady-state friction coefficient to variation in parameter values (σ_n, T, d, φ_c and φ_0, as well as progressively decreasing W_{sb}). Parametric analyses were performed for a wide range of slip rates from 0.001 μm/s to 1000 μm/s, using two fault geometries (A, B for distributed shear, and C, D for localized slip). For both geometries, the reference cases (thick grey lines) employs the denoted parameter values and for each other curve we changed one parameter. All the definitions and values of the parameters are listed in Table 3.

5.2.2. Simulation of Velocity Stepping Experiments

We next use the CNS model to investigate the transient shear deformation behavior, as observed in our v-stepping experiments. The experimental setup can be idealized as a spring-slider system (e.g. Chen & Spiers, 2016). From the initial response upon a perturbation in displacement rate, the apparent stiffness of the loading system measured 55 to 210 GPa/m. Taking a stiffness from this range, the model simulation will sometimes lead to stick-slips in the frictional regime, especially at relatively low velocities (e.g., for 0.3 μm/s < v < 10 μm/s), or when imposing a thin

shear band. Although the occurrence of stick-slip at low-v is consistent with the findings of Verberne et al. (2015), for calcite gouge sheared under the same T-σ_n-P_f conditions as used here, in the present experiments we consistently observed stable sliding. Therefore, in our model simulations we employed a stiffness of 500 GPa/m. Other model parameters are set to the same values as used for simulating steady state behavior (see Table 3). The initial displacement rate used in the model is set to 0.1 μm/s, beyond which we imposed the same v-stepping sequence as used in the experiments, allowing 0.5 mm of shear displacement in each v-interval. The initial shear stress and porosity were set according to the analytical expressions for steady state (Chen et al., 2017).

The model output alongside the experimental data are plotted as friction coefficient and porosity versus displacement in Fig. 10. For experiments conducted using $v < v_{cr}$, the predicted friction response shows a sharp drop followed by gradual restrengthening for the first three steps ($v \leq 0.01$ μm/s), comparing favorably with the experimental data (Fig. 10A). For each displacement rate tested, the model predicts continued compaction with increasing displacement. For $v \geq 0.003$ μm/s, when the porosity reaches the background level of φ_0, the shear strength shows a monotonic decay, without re-strengthening. A plot of friction vs sample (or particle) velocity (i.e. μ - v_s), termed a phase diagram by Gu et al. (1984), shows that the model simulation of downward v-steps defines a curve which is parallel to the interpolated experimental data (Fig. 11), with a gap that decreases with increasing slip rate.

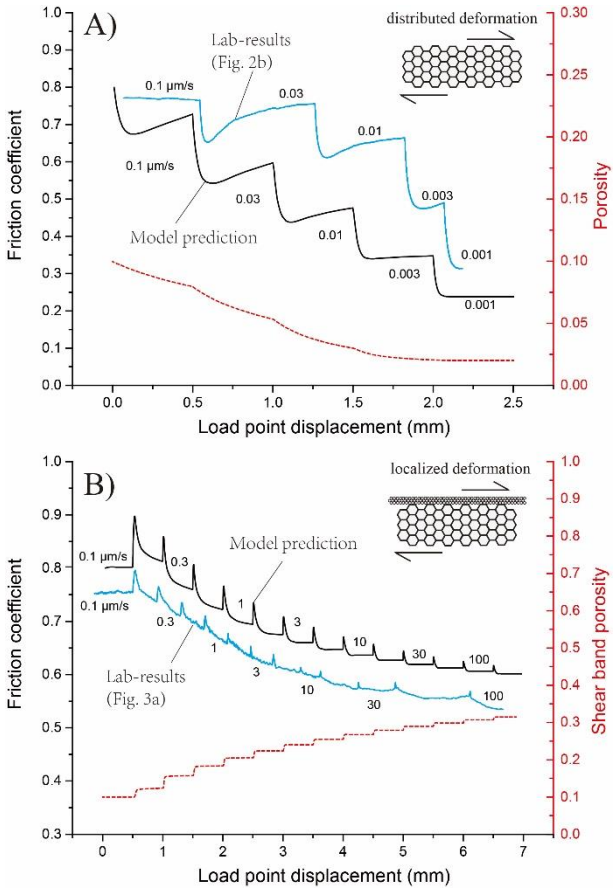

Figure 10. Predicted evolution of friction coefficient and porosity from the CNS model, to simulate A) the downward and B) upward v-stepping tests shown in Figs. 2 and 3, respectively. The experimental

data are added for comparison, with a slight extension of the x-axis for the comparing convenience.

The model output simulating the response in shear strength upon a step in displacement rate in v-stepping tests using $v > 0.1$ μm/s is strikingly consistent with the experimental data (Fig. 10B and 11). Firstly, all simulated upward *v*-steps showed a classical, RSF-type, frictional response, constituting *v*-weakening. Secondly, when using the same magnitude *v*-steps (1.75-fold), the difference in μ_{ss} before and after a v-step becomes less as the post-step *v* increases, implying an increase of the steady-state frictional rate dependence (i.e., the (a - b) value becomes less negative) with increasing *v*. Thirdly, the model output as well as the experimental data show a systematic decrease in the direct effect (i.e., the *a*-value) with increasing slip rate (see also the inset of Fig. 11). The same trend also describes the characteristic slip distance (i.e., the D_c value). Lastly, for $v \leq 3$ μm/s, friction-displacement curves representing the model as well as the experimental data do not reach steady state within 0.5 mm of displacement, whereas for $v > 10$ μm/s they do.

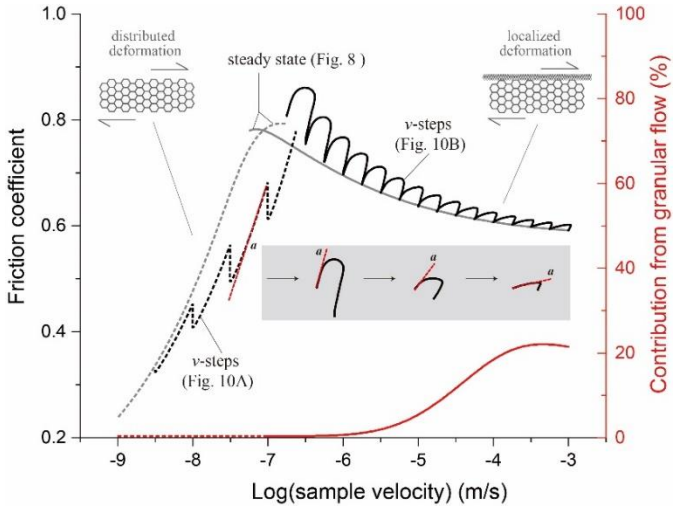

Figure 11. Friction-velocity phase diagram of the simulated *v*-steps shown in Fig. 10, with the predicted steady-state shear strength being added for comparison (in grey lines). Results from the friction and flow regimes, with distributed and localized deformation, are plotted in solid and dashed black lines, respectively. The red lines give the relative contribution from granular slip to the shear deformation. The grey inset illustrates the systematic decrease in the direct effect (or a-value) with increasing velocity.

The direct effect, defined as $a = d\mu/d(\ln v)$, can be directly measured as the slope of the instantaneous response in the μ-v_s phase diagram multiplied by ln(10) (see the inset of Fig. 11). We found that the direct effect continuously evolves from a flow-like process at low *v* to granular flow at high *v*. Specifically, for low velocity ($v < v_{cr}$), it measures as $a = a_{flow} = \mu/n$ where *n* is the stress exponent (eq. 2), while at high velocity ($v > v_{cr}$) its value gradually decreases from a_{flow} to $a_{\tilde{\mu}}$ which in the limit approaches the direct effect defined in in the RSF model (see Chen & Spiers, 2016). To further specify this, we investigate the relative contribution to shear strain accommodation of plastic flow vs. granular flow, at steady state (see the red curves in Fig. 11). In the flow regime ($v < v_{cr}$), shear deformation is fully accommodated by plastic flow, except that created small increment of porosity starts to play a role at $v > v_{dil}$. As slip rate increases, granular

flow plays an increasingly important role, ultimately accounting for up to 22% of the total shear strain rate. Their relative contribution determines the *a*-value, that is $a = \eta a_{\tilde{\mu}} + (1 - \eta)a_{flow}$, where $\eta = \dot{\gamma}_{gr}/(\dot{\gamma}_{gr} + \dot{\gamma}_{pl})$.

6. Discussion

6.1. Flow-to-Friction Transition and "Semi-brittle Flow" of Carbonates at 550 ˚C

In this study, we reported ring-shear experiments on layers of wet simulated calcite fault gouge sheared at 550 ˚C and 50 MPa effective normal stress conditions, at sliding velocities ranging from 0.001 to 300 μm /s. A plot of steady-state shear strength against sliding velocity (*v*) showed a transition with increasing *v* from *v*-strengthening to - weakening, characterized by a peak shear strength at a critical velocity v_{cr} = 0.1 mu/s (Fig. 4). Samples deformed at $v < 0.1$ μm/s are characterized by a dense, near-homogeneously deformed microstructure, compared with localized deformation in samples deformed at $v > 0.1$ μm/s. Our mechanical and microstructural findings are consistent with a transition with increasing slip rate from distributed, creep-controlled flow to localized, frictional slip beyond $v \approx 0.1$ μm/s. In the low-*v* flow regime, deformation is accommodated by compactive, plastic creep processes involving the entire width of the gouge layer. Towards higher slip rates ($v > 0.1$ μm/s), and in the case of localized slip, shear deformation by granular flow plays an increasingly important role. Despite the dramatic differences in the mechanical and microstructural characteristics between the 'slow' and the 'fast' shear deformation regimes, the creep mechanisms occurring between the grains may be modelled using an empirical constitutive law which represents a mixture of diffusion and dislocation creep.

The stress sensitivity or *n*-value determined for deformation in the flow regime showed an increase with increasing *v*, from 2.5 – 4.2 ($v \leq 0.01$ μm/s or $\dot{\gamma} \leq 1.25\times10^{-6}$ s^{-1}) to 8.8 – 87 ($v \rightarrow$ 0.1 μm/s, or $\dot{\gamma} \rightarrow 1.25\times10^{-5}$ s^{-1}) (Fig. 7). An increase of the *n*-value from 2.1 to 4.2 with increasing strain rate was reported from compression tests on dense calcite aggregates at 500 – 600 ˚C, by Bruhn et al. (1999). From the present post-mortem microstructures (Fig. 5, see also Verberne et al., 2017) and thickness measurements (Fig. S3), as well as the microphysical analysis of steady-state behavior (Fig. 8), we posit that the change in *n*-value (or slope in strain rate-stress curve) is caused by porosity development, or cavitation, at grain boundaries. Based on our microphysical model simulations (Fig. 8), intergranular cavitation is expected to become noticeable in the gouge shear mechanical properties when the sliding velocity overcomes the dilatancy velocity v_{dil}. With further increasing *v*, cavitation continues until the critical velocity v_{cr} is reached, which demarcates the flow-to-friction transition (Fig. 4) accompanied by the change from stable to unstable slip. Relatively high *n*-values and the development of porosity have also been observed in creep-type experiments on synthetic feldspar and granitoid rocks, conducted under conditions simulating the BDT (Rybacki et al., 2008; Delle Piane et al., 2009; Pec et al., 2016), and is often referred to as 'semi-brittle flow' behavior (Fredrich et al., 1989; Nicolas et al., 2017). "Semi-brittleness" can be verified by the emergence of normal stress dependence of shear strength, which shows that at a higher normal stress it is feasible to have continued deformation by purely plastic flow (without dilatancy) at elevated strain rates and therefore a higher v_{dil} -value (Figs. 9A and 9C).

In the semi-brittle shear deformation regime, the transient response to a sudden drop in loading velocity displays a sharp drop in shear stress followed by a gradual rise to a new steady state (Fig. 2). This is like that expected from a frictional response. Such transient behavior has

been observed in simulated halite(-mica) gouges sheared at room temperature and slow slip rates (0.03 - 0.1 μm/s), as a precursor to a transition from *v*-strengthening to -weakening (Niemeijer & Spiers, 2005). From our modelling results it appears as if deformation in the semi-brittle regime remains fully plastic (i.e. > 99% contribution, Fig. 11), however, porosity development due to cavitation effectively leads to local stress enhancement hence enhanced creep rates, at grain contacts. In other words, the stress required to accommodate gouge shear deformation by dense plastic flow, at zero or at least at very low porosity, is higher than that required to generate porosity, and to advance deformation at elevated strain rates. This means that in the semi-brittle deformation regime, it is energetically more favorable to create porosity than to sustain plastic flow.

6.2. Microphysical Modelling and Comparison with Previous Models

Using constraints based on observed or measured properties of sheared calcite fault gouge, the CNS model employed here predicts a flow-to-friction transition consistent with the experimental data (Fig. 8). The CNS model distinguishes itself from previous constitutive models describing fault deformation in the friction/flow regime such as the two-mechanism model (Reinen et al., 1992; Chester, 1994; Estrin & Brechet, 1996; Nakatani, 2001; Beeler, 2009; Noda & Shimamoto, 2010; Shimamoto & Noda, 2014), because it is based on lab-derived observations of microphysical deformation processes.

From the point of view of fault rupture modelling, transient shear deformation behavior is more important than steady-state, since the velocities vary greatly during earthquake ruptures and, practically, a seismically-active fault is always in some transient stage of the earthquake cycle. We have shown that the CNS model can favorably predict transient responses to *v*-steps in the friction as well as the flow deformation regime (Figs. 10 and 11). In particular, the CNS model predicts RSF-like behavior within the "semi-brittle flow" regime, which is consistent with that predicted by the empirical model by Noda & Shimamoto (2010) who fitted a rate- and state-dependent flow law to data from shear experiments on halite conducted at high temperatures. Finally, besides the mechanical behavior, the CNS model predicts an increase in porosity with increasing slip rates across the flow-to-friction transition (Fig. 10). Of interest is that the onset of dilatation occurs at a velocity (v_{dil}) before the transition, which, as shall be discussed in the following, has important implications for natural fault deformation at the BDT conditions.

Recently, Aharonov & Scholz (2018) developed a physics-based constitutive law for rock friction, based on the microphysics of contact creep, using an exponential law, and the coupling with frictional heating (hereafter referred to the A&S model). By considering the temperature and stresses at asperities, which impact the direct rate dependence of friction (or *a*-value in the framework of RSF theory) their model can lead to local (flash) melting, and predict different deformation regimes as a function of slip rate. Significantly, the A&S model predictions are essentially similar to those of the CNS model (Chen et al., 2017; Chen & Niemeijer, 2017). More recently, Aharonov & Scholz (2019) have applied their model to higher temperature and pressure conditions and showed that a brittle-to-ductile transition (BDT) with increasing depth is a direct consequence of their model. The common foundation shared by the A&S and CNS models, is the limit in net grain contact area, or porosity beyond which shear deformation switches from creep-controlled flow to normal-stress dependent (or frictional) sliding. Thus, this porosity or grain contact area limit is crucial for the conditions pertaining to the flow-to-friction transition

hence the depth to the BDT.

6.3. Limitations and Future Work

A potentially crucial uncertainty which we have not yet considered is to what extent recrystallization (grain growth) occurred during or after shear deformation. As addressed in section 4, the grains in the bulk gouges deformed at $v < 0.1$ μm/s have likely grown with respect to the starting material, in the early hours of the experiments. In the frictional regime ($v > 0.1$ μm/s) one would expect a high porosity (c. 10 - 30%) in the active shear band due to the operation of granular flow (Fig. 8). However, the post-mortem microstructure of the shear band occasionally shows polygonal grains with straight boundaries and high-angle junctions, with a relatively low porosity (< 9%, Fig. 5C). We infer that the compacted structure could be developed by static recrystallization in the termination stage of the experiments. Based on the observed grain size distribution (d = 0.3 – 1.4 μm, with $\bar{d}$ ~0.8 μm, Fig.5) and a temperature profile upon cooling after the experiment (see supplement Fig. S6-A), we can estimate the maximum grain sizes prior to annealing, using the grain growth equation for porous calcite aggregates (e.g., Covey-Crump, 1997). Assuming initial grain sizes from 0.01 μm to 1.0 μm, the calculations predict that grain growth mostly occurs within the first 50 s cooling (Fig. S6). For grains with an initial size (d_0) smaller than 0.2 μm, the final sizes after cooling are more or less constant and close to ~ 0.45 μm (Fig. S6-B), whereas for grains with d_0 exceeding 0.2 μm the total growth in grain size is limited to 0.25 μm (Fig. S6-C). The predicted minimum grain size of 0.45 μm is roughly consistent with our final observation. Therefore, before terminating shearing, the shear bands may contain a portion of grains that were smaller than the observation and have a systematically smaller mean value ($\bar{d}$) by ~0.15 μm, with a small portion of grains (~10%) that could be smaller than 100 nm (Fig. S6-D). This variation in the $\bar{d}$-value does fall in the range of our parametric analyses. However, we cannot rule out that the dynamic grain size during active shear could be even smaller (Verberbe et al., 2019). To explore this issue, experiments stopped at short shear displacements, together with ad hoc quenching procedures, are required in the future.

From our experiments as well as the microphysical model it remains ambiguous as to how semi-brittle flow, local porosity development, and/or slip instability leads to the formation of a shear band (i.e., spontaneous slip localization and grain size reduction). We speculate that this process may be tied to the development of dilatancy in the semi-brittle flow regime ($v_{dil} < v < v_{cr}$). Rationalized from a microscopic point of view: cavities developed at grain boundaries will generate high local stresses, which, added to the already high shear stress around the transition, will cause grain breakage preferably at the cavitated points. As stress continues to build up and more cavities develop, a previously creeping gouge can readily dilate from these cavities, leading to the emergence of strain localization and therefore the incipience of a shear band. In other words, it is the inability of semi-brittle flow to maintain the contiguity of a creeping gouge layer that leads to local disaggregation and thus the formation of shear band. Previous laboratory and numerical modelling studies also showed, in general, that shear localization occurs due to the presence of local heterogeneities, such as those in porosity and grain size distribution (Hadizadeh et al., 2010, 2015; Nübel & Huang, 2004), which could potentially lead to the ductile-to-brittle transition. Of course, a continuous flow-to-friction transition, together with the associated microstructural evolution (i.e., localization and grain size reduction), occurs spontaneously in both laboratory and natural shear zones (Platt & Behr, 2011; Wehrens et al., 2017), which is not yet

captured by the present model and will be considered in future work.

6.4. Implications for Fault Rupture Dynamics within the BDT Zone

Based on the present experimental and microphysical modelling results we sketch a diagram showing the shear strength-depth profile of a carbonate fault (Fig. 12A), with the expected fault rupture dynamics in the brittle-to-ductile transition (BDT) zone (Fig. 12B). For simplicity, the change of shear strength with increasing depth was predicted using the same model (i.e., the case of localized slip), but taking two constant loading velocities (10^{-10} and 10^{-9} m/s) and a geotherm of 25 ˚C/km.

At shallow depths, the shear strength shows a near-linear increase with increasing depth, representing frictional behavior (Fig. 12A). The difference between slow and fast loading velocities indicates a transition from *v*-strengthening to *v*-weakening with increasing depth. As depth increase, the peak strength on the profile marks the friction-to-flow transition (Fig. 12A). As embodied in the CNS model, this transition depth depends not only on the loading velocity but also on fault zone structure such as grain size and shear zone thickness, as well as fault conditions such as the thermal and effective pressure gradients. The variation of this transition depth, resulting from a range of velocities which the fault could potentially experience in an earthquake cycle, then defines the width of the BDT zone (see the grey zone in Fig. 12A).

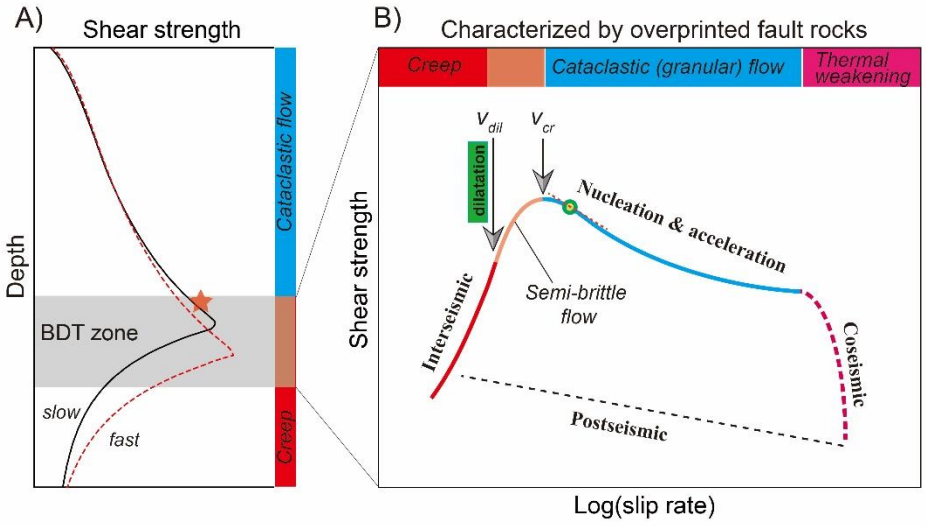

Figure 12. Diagrams illustrating (A) the shear strength-depth profile of a carbonate fault zone over the crustal depth at fast and slow velocities, and (B) the strength-velocity profile showing the dynamic of an earthquake that nucleates within the brittle-ductile transition (BDT) zone.

When an earthquake nucleates from a fault patch (or asperity) at the base of the seismogenic zone (see the red star in Fig. 12A), which is usually considered to be the upper bound of the BDT zone, it is expected that the fault patch will undergo a transition from stable, ductile flow over a wide shear zone, to unstable, localized frictional slip by cataclastic (granular) flow, involving a wide range of slip rates (see the thick line in Fig. 12B). Before the transition, the fault will first show semi-brittle flow behavior accompanied by the onset of dilatation as described in the earlier sections. Besides the evidence from laboratory experiments, similar mechanical and microstructural characteristics have also been observed in ductile fault rocks collected from

natural shear zones exhumed from the aseismic/seismic transition depths (25 - 35 km, Regenauer-Lieb, 1999; Shigematsu et al., 2004; Fusseis & Handy, 2008; Fusseis et al., 2009; Menegon et al., 2015; Platt et al., 2018; Gilgannon et al., 2017), sometimes using different terminologies such as "ductile rupture", "dilatant plasticity", "dilatant microcracking" and "creep cavitation". Our microphysical modelling predicts that "semi-brittle flow" occurs over a velocity range from the onset of dilatation until the transition to friction ($v_{dil} < v < v_{cr}$). An important implication is that the mechanical and microstructural features can be taken as indicators of the (aseismic) acceleration stage for a seismogenic fault to produce an instability at higher slip rates.

As the fault accelerates and continues to dilate at $v > v_{cr}$, its shear strength decreases, and an earthquake nucleates. However, as the fault just transitions into the *v*-weakening regime, the initial minimum nucleation size will be rather large since (a - b) has only a small negative value. However, as the fault accelerates further, (a - b) becomes more negative and this size will shrink until it reaches its minimum size at the steepest point in Fig. 12B, indicated by the red circle. As the slip area increases beyond the critical nucleation size, the rupture propagates and runaway slip occurs (Scholz, 2002). Finally, as the slip runs away to the coseismic regime (~1 m/s), some thermal weakening mechanisms such as flash heating will start to play a role (Niemeijer et al., 2012, Di Toro et al., 2011), leading to dramatic weakening. For a fault cutting carbonate rocks, one of the candidate mechanisms is grain boundary sliding with accommodation by diffusion creep (De Paola et al., 2015). Implementing this mechanism to explain carbonate dynamic weakening is a natural extension of the present model (i.e., simply using different creep law and with high temperature generated by frictional heating) and is in progress.

Finally, as discussed above, within the BDT zone the deformation and failure modes might switch between ductile non-localized plastic flow and brittle-localized patterns within the timeframe of earthquake cycles. The resultant fault rocks will be characterized by repeated overprinting of different deformation processes, specifically interseismic mylonitization, subseismic cataclasis and localization, and coseismic melting or superplasticity. These include pseudotachylyte overprinted with mylonitic deformation, mylonitized cataclasite, and cataclasite containing mylonite clasts (e.g., Takagi et al., 2000; Fusseis et al., 2009; Frost et al., 2011; Fagereng, 2011; Wehrens et al., 2016, 2017; Wintsch & Yeh, 2013). It is noteworthy that what is more commonly seen in outcrops are different layers of fault rocks coexisting across the fault zone (mylonite, cataclasite, pseudotachylyte, and fault gouge), which might form separately in different scenarios (e.g., along with the exhumation of the fault toward the surface).

7. Conclusions

In this study, we performed constant-velocity and velocity-stepping tests on layers of simulated calcite fault gouge at 550 ˚C, 50 MPa effective normal stress, and 100 MPa fluid pressure conditions, with slip rates covering almost six orders of magnitude (0.001 – 300 μm/s). The shear strength observed at these velocities shows a flow-to-friction transition within increasing slip rates, with a critical velocity (v_{cr}) of 0.1μm/s.

Distinct microstructures were displayed in the two regimes. In the flow regime (v < 0.1 μm/s), the gouge is well compacted, displaying a progressive homogeneous texture as slip rate decreases, while in the frictional regime ($v \geq$ 0.1 μm/s), a localized shear band was developed. A stress sensitivity with approximate *n*-values of 2.5 – 8.8 was recognized for the flow regime, which, in combination with the characteristic microstructure (i.e. compacted, polygonal grains with high

junction angles, some with subtle elongation), and CPO pattern observed, suggests deformation by a mixture of dislocation and diffusion creep. The same creep mechanism was inferred to also occur in the friction regime but is expected to accommodate only a part of the shear deformation, with the rest accommodated by granular flow which generates porosity and in turn enhances local stress and creep rate.

Incorporating the microstructures and inferred creep mechanisms, the microphysical model (CNS model) reproduces the steady-state shear strength profile showing the transition from flow to friction with increasing slip rate, as well as the transient flow/friction behavior in the flow/friction regime. In the frictional regime ($v > v_{cr}$), the model predicts typical v-weakening behavior; as velocity increases, there is a systematic decrease in the absolute value of (a - b), the a- and D_c- values, as velocity increases. The flow regime can be divided into two sub-regimes, separating from a velocity for the onset of dilatation (v_{dil}). At $v < v_{dil}$, the fault deforms by pure plastic flow following a power law, while at $v > v_{dil}$, the fault deforms by "semi-brittle flow", characterized by high stress sensitivity and a transient behavior similar to the RSF frictional behavior. All the predictions are generally consistent with the observations from experiments.

Implications for the dynamics of earthquake ruptures at the brittle-to-ductile transition zone are made based on the results from present experiments and microphysical model. In particular, our results show that the "semi-brittle flow" is occurring at velocities ranging from v_{dil} to v_{cr} and is linked to the opening of transient micro-porosity (or cavitation). As applied to a natural carbonate fault zone, the characteristics of the "semi-brittle" flow behavior sheds considerable insights for earthquake nucleation at the base of the seismogenic zone, i.e. as indicators of a precursory phase.

Acknowledgements

We thank Tony van der Gon-Netscher, Ing. Floris van Oort, and Gert Kastelein for technical support, and Yongmei Shang and Xi Ma for assisting with the EBSD analyses. We thank Prof. Chris Spiers and Prof. Hans De Bresser for discussions. This project is funded by the European Research Council, grant SEISMIC (335915), and by the Dutch Research Council, VIDI grant (854.12.011), awarded to ARN. BAV was supported by JSPS KAKENHI grant #19K14823. Experimental raw data and microphysical models with input data are all freely available through: https://doi.org/10.4121/uuid:63a7dbde-e223-43ad-b184-bc7f111f883c.

Reference

1. Aharonov, E., & Scholz, C. H. (2018). A physics-based rock friction constitutive law: Steady state friction. Journal of Geophysical Research, 123, 1591–1614.
2. Aharonov, E., & Scholz, C. H. (2019). The brittle-ductile transition predicted by a physics ‐ based friction law. JGR, 124, 2721–2737.
3. Blanpied, M. L., Lockner, D. A., & Byerlee, J. D. (1995). Frictional slip of granite at hydrothermal conditions. Journal of Geophysical
4. Research, 100(B7), 13,045 ‐ 13,064.
5. Beeler, N.M. (2009). Constructing constitutive relationships for seismic and aseismic fault slip, Pure and Applied geophysics, 166, 1775–1798.
6. Bestmann, M., Pennacchioni, G., Nielsen, S., Göken, M., & de Wall H. (2012). Deformation and ultrafine dynamic recrystallization of quartz in pseudotachylyte-bearing brittle faults: A matter of a few seconds. J. Struct. Geol., 38, 21-38.

7. Bos, B., & Spiers, C. J. (2002). Fluid-assisted healing processes in gouge bearing faults: Insights from experiments on a rock analogue system. Pure and Applied Geophysics, 159, 2537–2566.
8. Brace, W. F., & Kohlstedt, D. L. (1980). Limits on lithospheric stress imposed by laboratory experiments. Journal of Geophysical Research, 85(B11), 6248–6252.
9. Brantut, N., Heap, M. J., Meredith, P. G. &Baud, P. (2013). Time dependent cracking and brittle creep in crustal rocks: A review. J. Struct. Geol., 52, 17–43.
10. Bruhn, D. F., Olgaard, D. L., & Dell'Angelo, L. N. (1999). Evidence of enhanced deformation in two-phase rocks: Experiments on the rheology of calcite-anhydrite aggregates. Journal of Geophysical Research, 104, 707–724.
11. Chen, J., & Spiers, C. J. (2016). Rate and state frictional and healing behavior of carbonate fault gouge explained using microphysical model. Journal of Geophysical Research, 121, 8642–8665.
12. Chen, J., & Niemeijer, A. R. (2017). Seismogenic potential of a gouge-filled fault and the criterion for its slip stability: Constraints from a microphysical model. Journal of Geophysical Research, 122, 9658–9688.
13. Chen, J., Niemeijer, A. R., & Spiers, C. J. (2017). Microphysically derived expressions for rate‐and‐state friction parameters, a, b, and Dc. Journal of Geophysical Research, 122, 9627–9657.
14. Chen, J., van den Ende, M. P. A., & Niemeijer, A. R. (2020). Microphysical model predictions of fault restrengthening under room‐humidity and hydrothermal conditions: From logarithmic to power‐law healing. Journal of Geophysical Research, 125, e2019JB018567. https://doi.org/10.1029/2019JB018567
15. Chester, F. M. (1988). The brittle-ductile transition in a deformation-mechanism map for halite. Tectonophysics, 154, 125–136.
16. Chester, F. M. (1994). Effects of temperature on friction: Constitutive equations and experiments with quartz gouge. Journal of Geophysical Research, 99(B4), 7247–7261.
17. Chester, F. M., & Higgs, N. G. (1992). Multimechanism friction constitutive model for ultrafine quartz gouge at hypocentral conditions. JGR: Solid Earth, 97(B2), 1859-1870.
18. Covey-Crump, S. J. (1997). The normal grain growth behaviour of nominally pure calcite aggregates. Contrib. Mineral. Petrol. 129, 239–254.
19. De Bresser, J. H. P., Evans, B. & Renner, J. (2002). On estimating the strength of calcite rocks under natural conditions. Geol. Soc. London Spec. Pub. 200, 309–329.
20. De Paola, N., Holdsworth, R.E., Viti, C., Collettini, C., & Bullock, R. (2015). Can grain size sensitive flow lubricate faults during the initial stages of earthquake propagation?. Earth and Planetary Science Letters, 431, 48–58.
21. Delle Piane, C., Wilson, C. J. L. & Burlini L. (2009). Dilatant plasticity in high-strain experiments on calcite‐muscovite aggregates. J. Struct. Geol., 31(10), 1084–1099, doi:10.1016/j.jsg.2009.03.005.
22. Den Hartog, S. A. M., Niemeijer, A. R., & Spiers, C. J. (2013). Friction on subduction megathrust faults: Beyond the illite‐muscovite transition. Earth and Planetary Science Letters, 373, 8–19.
23. Di Toro, G., Han, R., Hirose, T., De Paola, N., Nielsen, S., Mizoguchi, K., Ferri, F., Cocco, M., & Shimamoto T. (2011). Fault lubrication during earthquakes. Nature, 471, 493–499.

24. Drury, M. R., Humphreys, F. J. & White, S. H. (1985). Large strain deformation studies using polycrystalline magnesium as a rock analogue. Part II: dynamic recrystallisation mechanisms at high temperatures. Phys. Earth Plan. Int., 40, 208-222.
25. Estrin, Y. & Brechet, Y. (1996). On a model of frictional sliding. Pure Appl. Geophys,. 4, 745–762.
26. Fagereng, A. (2011). Geology of the seismogenic subduction thrust interface. Geological Society, London, Special Publications 359, 55-76.
27. Fredrich, J. T., Evans, B., Wong, T.-F. (1989). Micromechanics of the brittle to plastic transition in Carrara marble. J. Geophys. Res., 94, 4129 - 4145
28. Frost, E., Dolan, J., Ratschbacher, L., Hacker, B., & Seward, G. (2011). Direct observation of fault zone structure at the brittle-ductile transition along the Salzach-Ennstal-Mariazell-Puchberg fault system, Austrian Alps. J. Geophys. Res., 116, B02411, doi:10.1029/2010JB007719.
29. Fusseis, F., & Handy, M.R. (2008). Micromechanisms of shear zone propagation at the brittle-viscous transition. J. Struct. Geol. 30, 1242-1253.
30. Fusseis, F., Regenauer-Lieb, K., Liu, J., Hough, R. M. & De Carlo, F. (2009). Creep cavitation can establish a dynamic granular fluid pump in ductile shear zones. Nature 459, 974–977.
31. Gifkins, R. C. (1970). Optical microscopy of metals, Elsevier, New York.
32. Gilgannon, J., Fusseis, F., Menegon, L., Regenauer-Lieb, K., & Buckman, J. (2017). Hierarchical creep cavity formation in an ultramylonite and implications for phase mixing. Solid Earth, 85194, 1193–1209.
33. Gu, J. C., Rice, J. R., Ruina, A. L., & Tse, S. T. (1984). Slip motion and stability of a single degree of freedom elastic system with rate and state dependent friction. Journal of the Mechanics and Physics of Solids, 32, 167–196.
34. Hadizadeh, J., Sehhati, R., & Tullis, T. (2010). Porosity and particle shape changes leading to shear localization in small-displacement faults. J. Struct. Geol., 32, 712-720.
35. Hadizadeh, J., Tullis, T., White, J. C., & Konkachbaev, A. I. (2015). Shear localization, velocity weakening behavior, and development of cataclastic foliation in experimental granite gouge. Journal of Structural Geology, 71, 86-99.
36. Hayman, N. W., & Lavier, L. L. (2014). The geologic record of deep episodic tremor and slip. Geology 42 (3), 195–198.
37. Herwegh, M., Xiao, X., & Evans, B. (2003). The effect of dissolved magnesium on diffusion creep in calcite. Earth Planet. Sci. Lett. 212, 457-470.
38. Holdsworth, R. E., Stewart, M., Imber, J. & Strachan, R. A. (2001). The structure and rheological evolution of reactivated continental shear zones: a review and case study. Geol. Soc. London Spec. Publ. 184, 115–137.
39. Imber, J., Holdsworth, R. E., Smith, S. A. F., Jefferies, S. P. & Collettini, C. (2008). Frictional-viscous flow, seismicity and the geology of weak faults: a review and future directions. Geol. Soc. London Spec. Publ. 299, 151–173.
40. Jiang, J., & Lapusta, N. (2016). Deeper penetration of large earthquakes on seismically quiescent faults. Science, 352(6291), 1293–1297.
41. Kawamoto, E., & Shimamoto, T. (1997). Mechanical behavior of halite and calcite shear zones from brittle to fully-plastic deformation and a revised fault model, in Proceedings of

the 30th International Geological Congress, Beijing, China, 4–14 August 1996, vol. 14, pp. 89–105.3, VSP, Utrecht, Netherlands.

42. Lafrance, B., White, J. C., & Williams, P. F. (1994). Natural calcite c-axis fabrics: An alternate interpretation. Tectonophysics, 229, 1–18.
43. Meissner, R., & Strehlau, J. (1982). Limits of stresses in continental crusts and their relation to the depth-frequency distribution of shallow earthquakes. Tectonics, 1, 73–89.
44. Menegon, L., Fusseis, F., Stunitz, H., & Xiao, X. (2015). Creep cavitation bands control porosity and fluid flow in lower crustal shear zones. Geology 43, 227–230.
45. Nakatani, M. (2001). Conceptual and physical clarification of rate and state friction: Frictional sliding as a thermally activated rheology. Journal of Geophysical Research, 106(B7), 13,347–13,380.
46. Nicolas, A., Fortin, J., Regnet, J. B., Verberne, B. A., Plümper, O., Dimanov, A., Spiers, C. J., & Guéguen, Y. (2017). Brittle and semibrittle creep of Tavel limestone deformed at room temperature. J. Geophys. Res., 122, 4436–4459.
47. Niemeijer, A. R. & Spiers, C. J. (2005). Influence of phyllosilicates on fault strength in the brittle-ductile transition: Insights from rock analogue experiments. In “High Strain Zones: Structure and Physical Properties”, D. Bruhn and L. Burlini (eds) Special Publication. Geological Society of London, pp. 303-327.
48. Niemeijer, A. R., & Spiers, C. J. (2006). Velocity dependence of strength and healing behaviour in simulated phyllosilicate-bearing fault gouge. J. Geophys. Res., 427, 231–253.
49. Niemeijer, A. R., & Spiers, C. J. (2007). A microphysical model for strong velocity weakening in phyllosilicate‐bearing fault gouges. Journal of Geophysical Research, 112, B10405. https://doi.org/10.1029/2007JB005008
50. Niemeijer, A. R., Spiers, C. J., & Peach, C. J. (2008). Frictional behavior of simulated quartz fault gouges under hydrothermal conditions: Results from ultra-high strain rotary shear experiments. Tectonophysics 460, 288-303.
51. Niemeijer, A., Di Toro, G., Smith, S. A. F., Griffith, A. W., Bistacchi, A., & Nielsen S. (2012). Inferring earthquake physics and chemistry using an integrated field and laboratory approach. J. Struct. Geol., 39, 2–36.
52. Niemeijer, A. R., Boulton, C., Toy, V. G., Townend, J., & Sutherland, R. (2016). Large-displacement, hydrothermal frictional properties of DFDP-1 fault rocks, Alpine Fault, New Zealand: Implications for deep rupture propagation, J. Geophys. Res., 121, 624–647.
53. Niemeijer A. R. (2018). Velocity-dependent slip weakening by the combined operation of pressure solution and foliation development. Scientific Reports, 8: 4724, DOI:10.1038/s41598-018-22889-3.
54. Noda, H., & Shimamoto, T. (2010). A rate- and state-dependent ductile flow law of polycrystalline halite under large shear strain and implications for transition to brittle deformation, Geophys. Res. Lett., 37, L09310, doi:10.1029/2010GL042512.
55. Nübel, K., & Huang, W. (2004). A study of localized deformation pattern in granular media. Comput. Method Appl. M., 193, 2719-2743.
56. Pec, M., Stünitz, H., Heilbronner, R., & Drury, M. (2016). Semi-brittle flow of granitoid fault rocks in experiments. J. Geophys. Res., 121, 1677–1705.
57. Platt, J. P., & Behr, W. M. (2011). Grain size evolution in ductile shear zones: Implications for strain localization and the strength of the lithosphere. J. Struct. Geo., 33, 537 – 550.

58. Platt, J. P., Xia, H., & Schmidt, W. L. (2018). Rheology and stress in subduction zones around the aseismic/seismic transition. Progress in Earth and Planetary Science, 5: 24, https://doi.org/10.1186/s40645-018-0183-8.
59. Prior, D. J., Boyle, A. P., Brenker, F., Cheadle, M. C., Day, A., Lopez, G., Purezzo, L., Potts, G. J., Reddy, S., Spiess, R., Timms, N. E., Trimby, P.W., Wheeler, J., & Zetterstrom, L. (1999). The application of electron backscatter diffraction and orientation contrast imaging in the SEM to textural problems in rocks. American Mineralogist 84, 1741-1759.
60. Regenauer-Lieb, K. (1999). Dilatant plasticity applied to Alpine collision: ductile void growth in the intraplate area beneath the Eifel volcanic field. Geodynamics 27, 1–21.
61. Reinen, L. A., Tullis, T. E. & Weeks, J. D. (1992). Two-mechanism model for frictional sliding of serpentinite. Geophys. Res. Lett., 19(15), 1535–1538.
62. Rutter, E. H., Casey, M., & Burlini, L. (1994). Preferred crystallographic orientation development during the plastic and superplastic flow of calcite rocks. J. Struct. Geol., 16, 1431–1446.
63. Rybacki, E., Wirth, R. & Dresen, G. (2008). High-strain creep of feldspar rocks; implications for cavitation and ductile failure in the lower crust. Geophys. Res. Lett. 35, L04304.
64. Schmid, S. M., Boland, J. N. & Paterson, M. S. (1977). Superplastic flow in finegrained limestone. Tectonophysics, 43, 257–291.
65. Schmid, S. M., Panozzo, R. & Bauer, S. (1987). Simple shear experiments on calcite rocks; theology and microfabric. Journal of Structural Geology, 9, 747-778.
66. Schmid, S. M., Paterson, M. S. & Boland, J. N. (1980). High temperature flow and dynamic recrystallization in Carrara Marble. Tectonophysics, 65, 245- 280.
67. Scholz, C.H. (1988). The brittle-plastic transition and the depth of seismic faulting. Geol. Rundsch., 77, 319–328.
68. Scholz, C. H. (2002). The mechanics of earthquakes and faulting (2nd edition). Cambridge: Cambridge University Press.
69. Shigematsu, N., Fujimoto, K., Ohtani, T. & Goto, K (2004). Ductile fracture of fine-grained plagioclase in the brittle-plastic transition regime: implication for earthquake source nucleation. Earth Planet. Sci. Lett. 222, 1007–1022.
70. Shimamoto, T. (1986). Transition between frictional slip and ductile flow for halite shear zones at room temperature. Science 231, 711–714.
71. Shimamoto, T., & Noda, H. (2014). A friction to flow constitutive law and its application to a 2-D modelling of earthquakes, J. Geophys. Res., 119, 8089–8106.
72. Sibson, R.H. (2003). Thickness of the seismic slip zone. Bull. Seismol. Soc. Am., 93, 1169–1178.
73. Stipp, M., Stünitz, H., Heilbronner, R., & Schmid, S. M. (2002). The Eastern Tonale fault zone: A “natural laboratory” for crystal plastic deformation of quartz over a temperature range from 250°C to 700°C. J. Struct. Geol., 24, 1861–1884.
74. Takagi, H., Goto, K. & Shigematsu, N. (2000). Ultramylonite bands derived from cataclasite and pseudotachylite in granites, northeast Japan. J. Struct. Geol. 22, 1325–1339.
75. Takahashi, M., van den Ende, M. P. A., Niemeijer, A. R., & Spiers, C. J. (2017). Shear localization in a mature mylonitic rock analog during fast slip. Geochem. Geophys. Geosyst., 18, doi:10.1002/2016GC006687

76. Tse, S. T., & Rice, J. R. (1986). Crustal earthquake instability in relation to the depth variation
of frictional slip properties. J. Geophys. Res. 91 (B9), 9452.
Ueda, T., Obata, M., Di Toro, G., Kanagawa, K., & Ozawa, K. (2008). Mantle earthquakes frozen in mylonitized ultramafic pseudotachylytes of spinel‐lherzolite facies. Geology, 36(8), 607–610. https://doi.org/10.1130/G24739A.1
77. Verberne, B. A., Niemeijer, A. R., De Bresser, J. H. P., & Spiers, C.J. (2015). Mechanical behavior and microstructure of simulated calcite fault gouge sheared at 20–600 ^{o}C: Implications for natural faults in limestones. J. Geophys. Res., 120, 8169–8196.
78. Verberne, B. A., Chen, J., Niemeijer, A. R., de Bresser, J. H. P., Pennock, G. M., Drury, M. R., & Spiers, C. J. (2017). Microscale cavitation as a mechanism for nucleating earthquakes at the base of the seismogenic zone. Nat. Commun., 8, 1645.
79. Verberne, B. A., Plümper O., & Spiers, C. J. (2019). Nanocrystalline principal slip zones and their role in controlling crustal fault rheology. Minerals, 9, 328, doi:10.3390/min9060328
80. Vermeer, P.A., & De Borst, R. (1984). Non-associated plasticity for soils, concrete and rock. HERON 29 (3).
81. Walker, A. N., Rutter, E. H. & Brodie, K. H. (1990). Experimental study of grain-size sensitive flow of synthetic, hot-pressed calcite rocks, in Deformation Mechanisms, Rheology and Tectonics, edited by R. J. Knipe and E. H. Rutter, Geol. Soc. Spec. Publ., 54, 259-284.
82. Wehrens, P., Baumberger, R., Berger, A., & Herwegh, M. (2017). How is strain localized in a meta-granitoid, mid-crustal basement section? Spatial distribution of deformation in the central Aar massif (Switzerland). J. Struct. Geol., 94, 47-67.
83. Wehrens, P., Berger, A., Herwegh, M., Peters, M., & Spillmann, T. (2016). Deformation at the frictional-viscous transition: evidence for cycles of fluid-assisted embrittlement and ductile deformation in the granitiod crust. Tectonophysics, 693, 66 – 84.
84. Wintsch, R. P., & Yeh, M. W. (2013). Oscillating brittle and viscous behavior through the earthquake cycle in the Red River Shear Zone: Monitoring flips between reaction and textural softening and hardening. Tectonophysics, 587, 46-62.

Table 1. Experiments and Related Key Parameters [a].

run	v (μm/s)	μ_{max}	x_{max} (mm)	μ_{ss}	$\Delta\mu_r$	x_{ss} (mm)	x_{final} (mm)
u513	300	0.99	0.74	0.365	0.007	4.1 - 7.4	7.4
u550-fast [b]	100	1.04	0.52	0.482	0.004	5.0 - 9.0	10.3
u603	30	1.07	1.10	0.588	0.010	5.0 - 7.3	7.3
u635	10	1.02	0.95	0.602	0.011	5.0 - 7.2	7.2
u550-slow [b]	10	0.91	0.70	0.548	0.002	4.0 - 5.2	5.2
u594	3.0	0.93	0.80	0.673	0.005	7.5 - 10.2	10.2
u507	1.0	0.83	0.55	0.634	0.011	5.0 - 7.3	7.3
u593	0.3	0.95	0.60	0.716	0.019	5.0 - 7.1	7.1
u516	0.1	1.02	0.90	0.802	0.002	5.0 - 7.8	7.8
u508	0.027	0.83	1.50	0.806	0.015	3.5 - 5.6	5.6
u499 [c]	1.0	0.84	0.45	0.625	0.006	3.5 - 5.4	10.7
continued by	1.0 → 0.54 → 0.3 → 1.0 → 0.30 → 0.1 → 1.0 → 3.0 → 10 → 54 → 100 μm/s						
μ_{ss}	0.625 | 0.603 | 0.610 | 0.601 | 0.613 | 0.630 | 0.613 | 0.563 | 0.516 | 0.476 | 0.427						
u502 [c]	0.1	0.83	1.42	0.761	0.005	5.0 - 7.2	22.0
continued by	0.1 → 0.175 → 0.3 → 0.54 → 1 → 1.75 → 3 → 5.4 → 10 → 17.5 → 30 → 54 → 100 → 175 → 300 μm/s						
μ_{ss}	0.761 | 0.742 | 0.715 | 0.691 | 0.664 | 0.644 | 0.624 | 0.608 | 0.588 | 0.577 | 0.568 | 0.554 | 0.488 | 0.522 | 0.520						
u517 [c]	0.1	1.02	0.90	0.807	0.015	4.2 - 7.2	7.8
continued by	0.1 → 0.01 μm/s						
μ_{ss}	0.807 | 0.700						
u597 [c]	0.1	1.00	1.60	0.759	0.041	4.0 - 6.2	8.6
continued by	0.1 → 0.03 → 0.01 → 0.003 μm/s						
μ_{ss}	0.759 | 0.766 | 0.764 | 0.549						
u605 [c]	0.1	0.90	1.30	0.782	0.004	5.0 - 6.0	8.5
continued by	0.1 → 0.03 → 0.01 → 0.003 → 0.001 μm/s						
μ_{ss}	0.782 | 0. 762 | 0.672 | 0.500 | 0.338						

[a]. v = imposed shear velocity, μ_{ss} = steady-state friction coefficient, $\Delta\mu_r$= standard deviation of the μ_{ss} measured, x_{ss} = the shear displacement (x) range used to measure the steady-state friction, μ_{max} = maximum (or apparent yield) friction coefficient, x_{max} = the x-position to measure the peak friction, and x_{final} = final shear displacement.

[b]. Results derived from the experiments performed by Verberne et al. (2017) under the same conditions.

[c]. Stable sliding at v = 0.1 μm/s was followed by v-steps, for which the μ_{ss} and $\Delta\mu_r$ values are displayed in Fig. 4.

Table 2. Proposed Constitutive Creep Laws of Calcite at High Temperature-Pressure Conditions [a]

	$logA$ ($s^{-1}\mu m^{-m} MPa^{-n}$)	E_a (kJ/mol)	n	m	Source
GSS	6.68	213	1.70	3.00	Schmid et al.(1977): regime 3
GSS	7.63	200	1.10	3.26	Herwegh et al. (2003)
GSS + GSI	2.00	190	3.33	1.34	Walker et al. (1990): intermediate σ/T
GSI	3.10	420	7.60	-	Schmid et al. (1980): regime 2
GSI	8.10	428	4.20	-	Schmid et al. (1980): regime 3
GSI	16.65	584	-	-	De Bresser (2002)

[a] GSS and GSI denote grain-size sensitive and grain-size insensitive creep, respectively. The constitutive creep laws proposed are either in a power form $\dot{\varepsilon} = Aexp\left(-\frac{E_a}{RT}\right)\frac{\sigma^n}{d^m}$ or an exponential from $\dot{\varepsilon} = Aexp\left(-\frac{E_a}{RT}\right) exp\left(\frac{\sigma}{B}\right)$, where T, σ and d are in units of K, MPa, and μm, respectively. The factor B is 2.43 MPa in the exponential law proposed by De Breser (2002).

Table 3. Microphysical Model Parameters and Values

Symbol	Description (unit)	Values [a]	Source
σ_n	effective normal stress	50 MPa	Present experiment
T	temperature	550 ℃	Present experiment
K	stiffness of a simulated fault	6×10^{11} Pa/m	This study
W	thickness of the homogeneous gouge layer	0.8 mm	Microstructure
d	nominal grain size of a homogeneous gouge layer	3 (2 – 4) μm	Microstructure
W_{sb}	shear band thickness in the case in localized slip	50 (30 – 100) μm	Microstructure
W_{bulk}	thickness of the bulk zone in the case of localized slip	0.8 mm- W_{sb}	Microstructure
d^{sb}	nominal grain size of the shear band	0.8 μm	Microstructure
d^{bulk}	grain size in the bulk layer	5.0 μm	Microstructure
φ_c	critical state porosity for granular flow	0.4	This study
φ_0	terminal porosity of a compacted gouge	0.02	Chen & Niemeijer (2017)
φ_{ini}	Initial porosity in both shear and bulk layer	0.10	This study
p	sensitivity parameter in porosity function	2.0	Spiers et al. (2004)
H	geometrical parameter for grain package	0.57	Chen & Spiers (2016)
$\tilde{\mu}^*$	grain boundary (gb) friction coefficient at 1 μm/s	0.45	This study
$\tilde{\mu}$	logarithmic rate dependence of gb friction	0.01	Chen & Niemeijer (2017)

[a] Values in the brackets give the variations for parametric analysis. Constant parameter values in the creep law are given in Table 2 (GSS + GSI, Walker et al., 1990).

Figure 1.

A)

P-compensation piston

Upper closure nut

Thermocouple

Upper sealing head

Fluid pressure

Cooling water

Teflon filler

Sheathed material

Monel vesel

Furnace with surrounding sheathed material

Lower sealing head

Thermocouple

Lower closure nut

B)

Stationary upper piston

Thermocouple

Retaining screw

Outer ring & inner ring

Gouge ring

Rotary lower piston

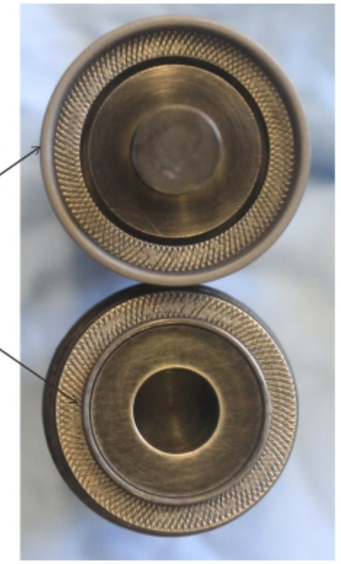

Top view

C)

Before experiment

After experiment

Figure 2.

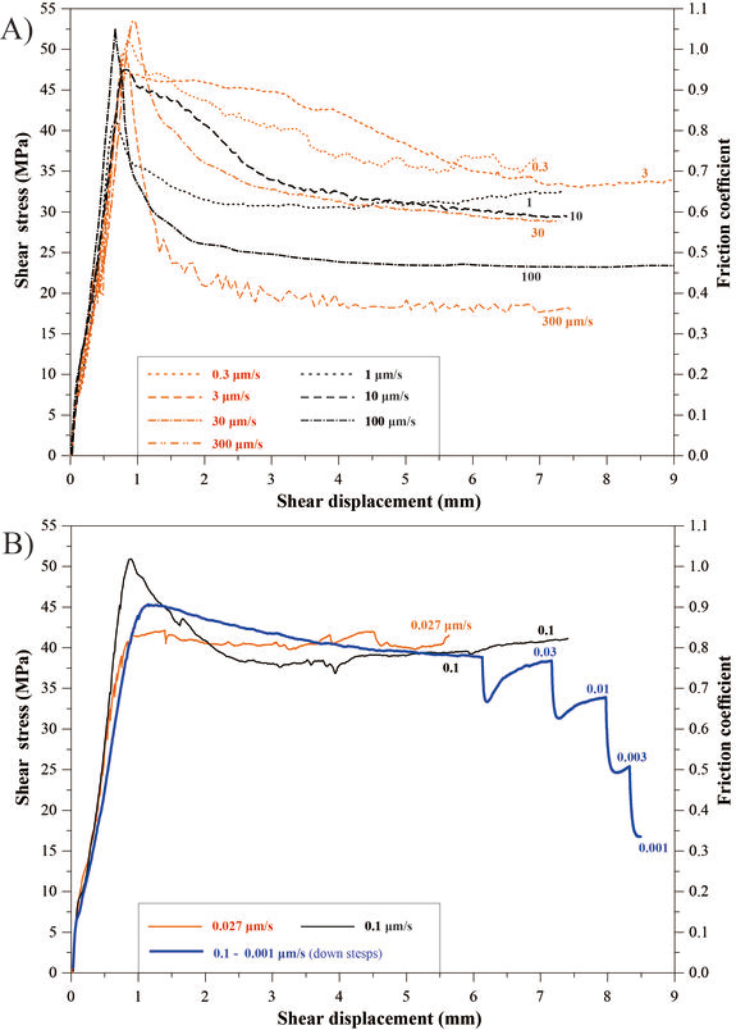
A)
Shear stress (MPa)
Friction coefficient
Shear displacement (mm)
0.3
3
1
10
30
100
300 μm/s
0.3 μm/s
1 μm/s
3 μm/s
10 μm/s
30 μm/s
100 μm/s
300 μm/s
B)
Shear stress (MPa)
Friction coefficient
Shear displacement (mm)
0,027 μm/s
0.1
0.1
0,03
0,01
0,003
0,001
0.027 μm/s
0.1 μm/s
0,1 - 0,001 μm/s (down steps)

Figure 3.

A)

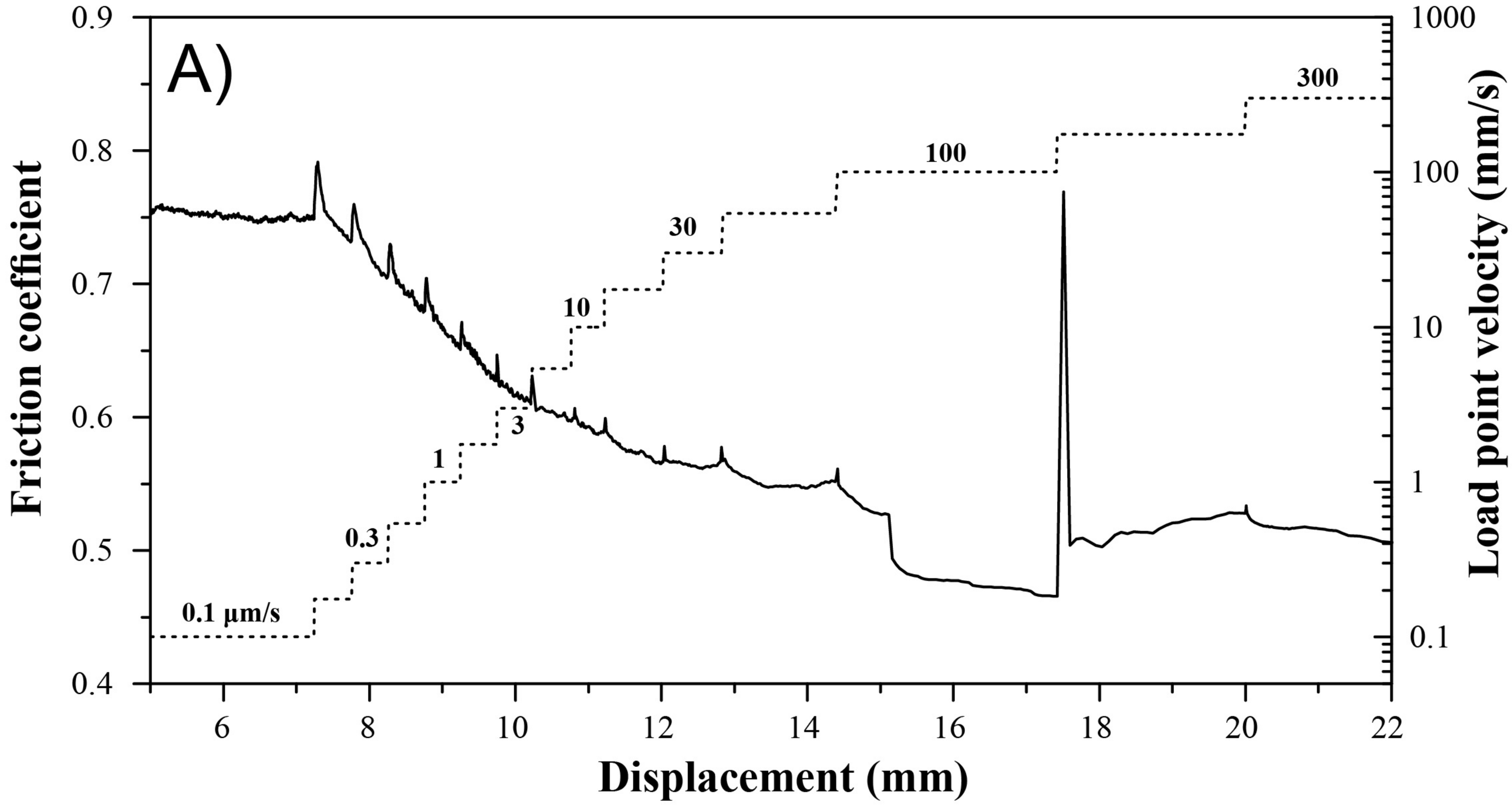
Friction coefficient
Load point velocity (mm/s)
Displacement (mm)
0.9
0.8
0.7
0.6
0.5
0.4
1000
100
10
1
0.1
6
8
10
12
14
16
18
20
22
0.1 µm/s
0.3
1
3
10
30
100
300

B)

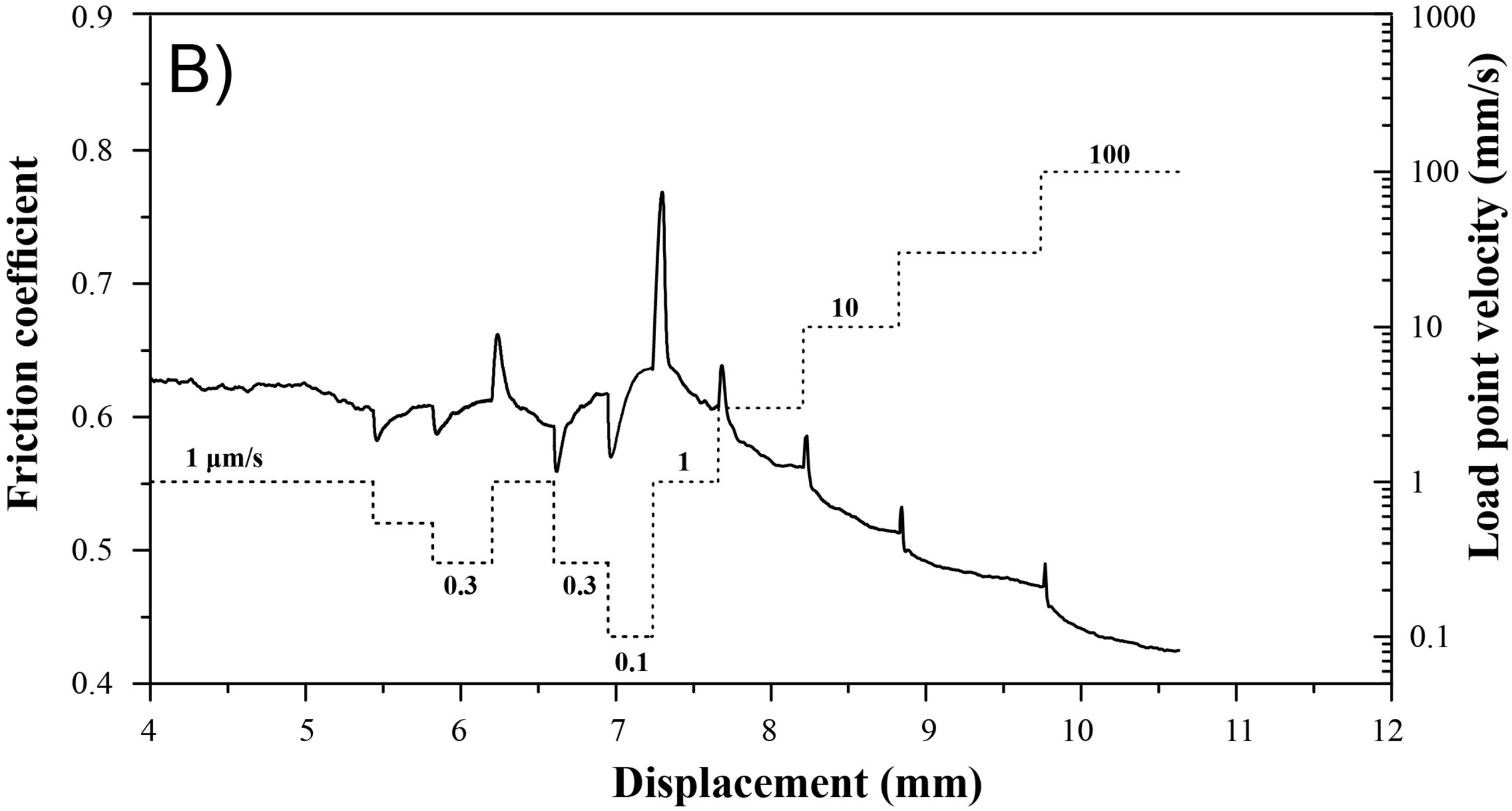
Friction coefficient
Load point velocity (mm/s)
Displacement (mm)
0.9
0.8
0.7
0.6
0.5
0.4
1000
100
10
1
0.1
4
5
6
7
8
9
10
11
12
1 µm/s
0.3
0.3
0.1
1
10
100

Figure 4.

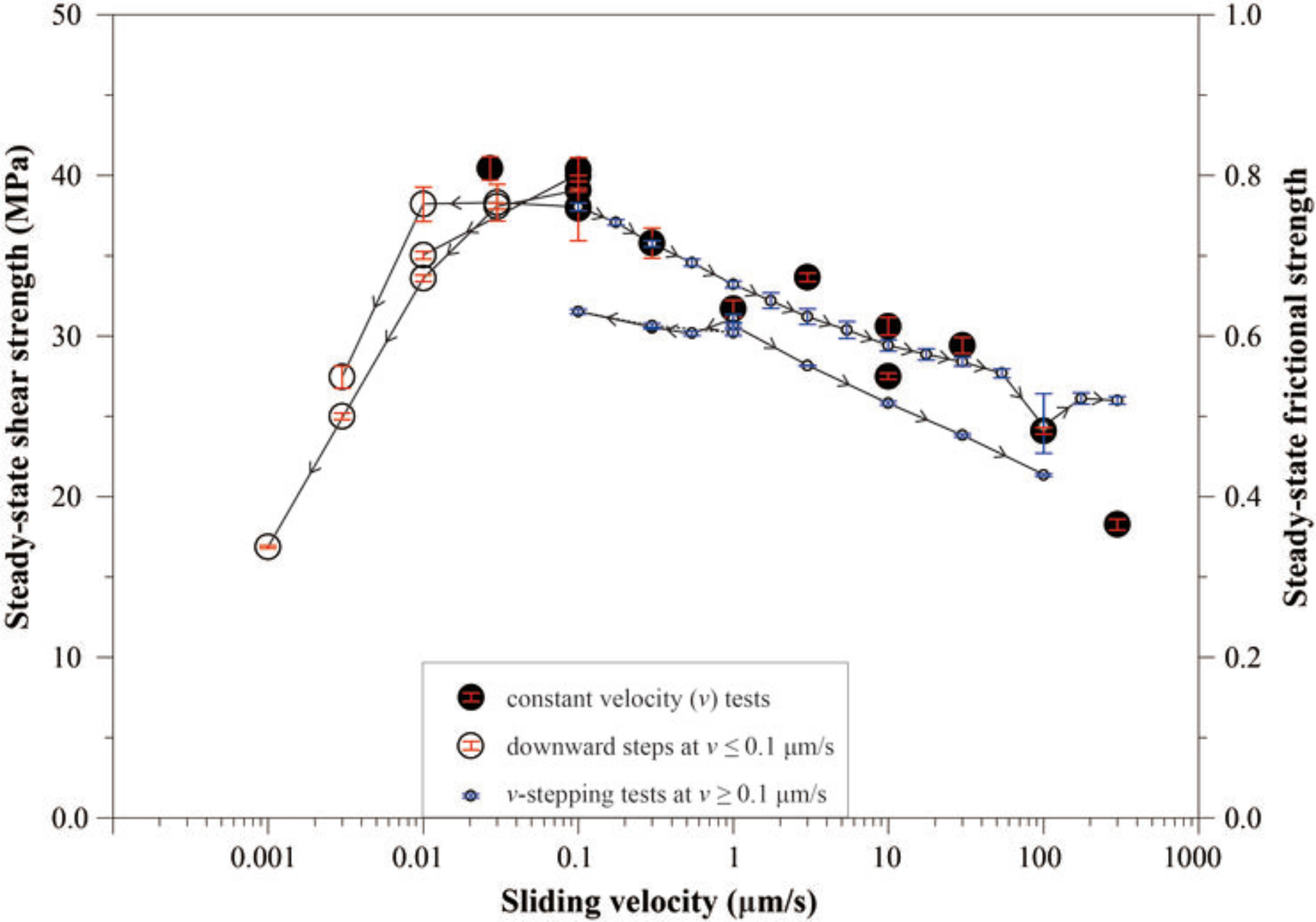
Steady-state shear strength (MPa)
Steady-state frictional strength
Sliding velocity (μm/s)
50
40
30
20
10
0.0
1.0
0.8
0.6
0.4
0.2
0.0
0.001
0.01
0.1
1
10
100
1000
constant velocity (v) tests
downward steps at v ≤ 0.1 μm/s
v-stepping tests at v ≥ 0.1 μm/s

Figure 5.

A)

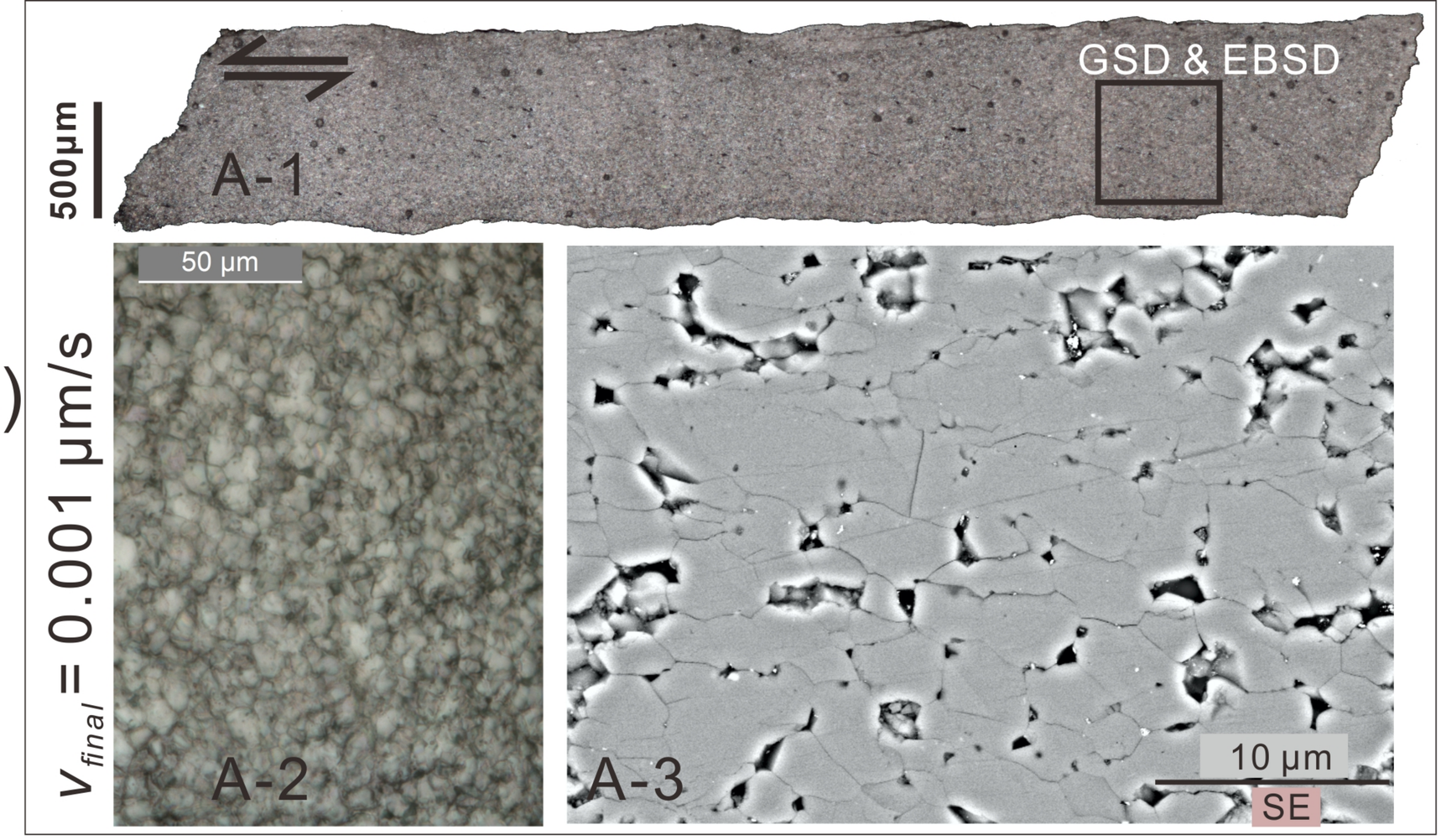
500μm
A-1
GSD & EBSD
v_{final} = 0.001 μm/s
50 μm
A-2
A-3
10 μm
SE

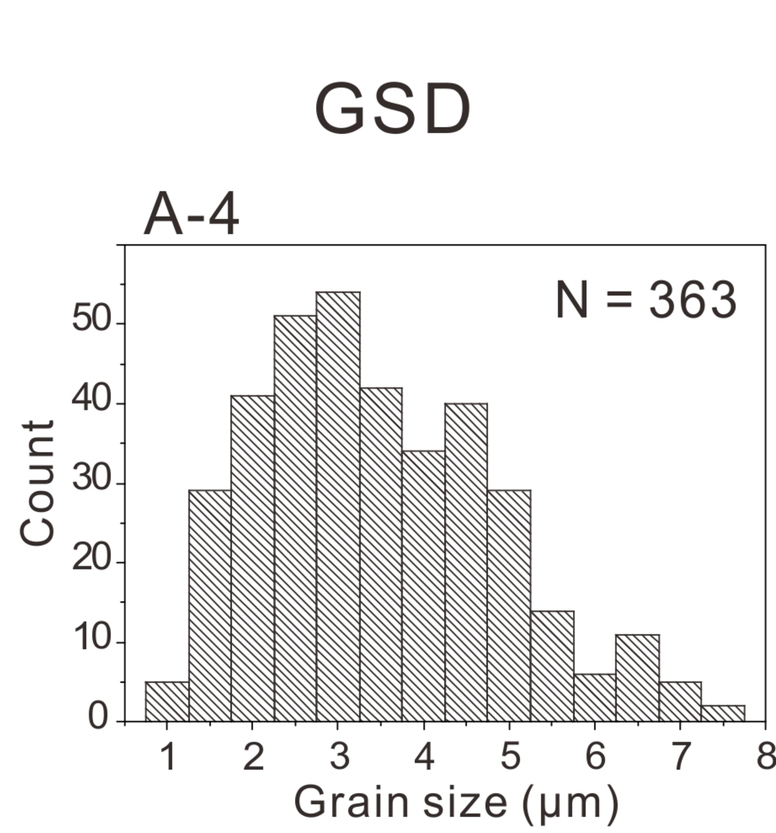
GSD
A-4
N = 363
Count
Grain size (μm)

B)

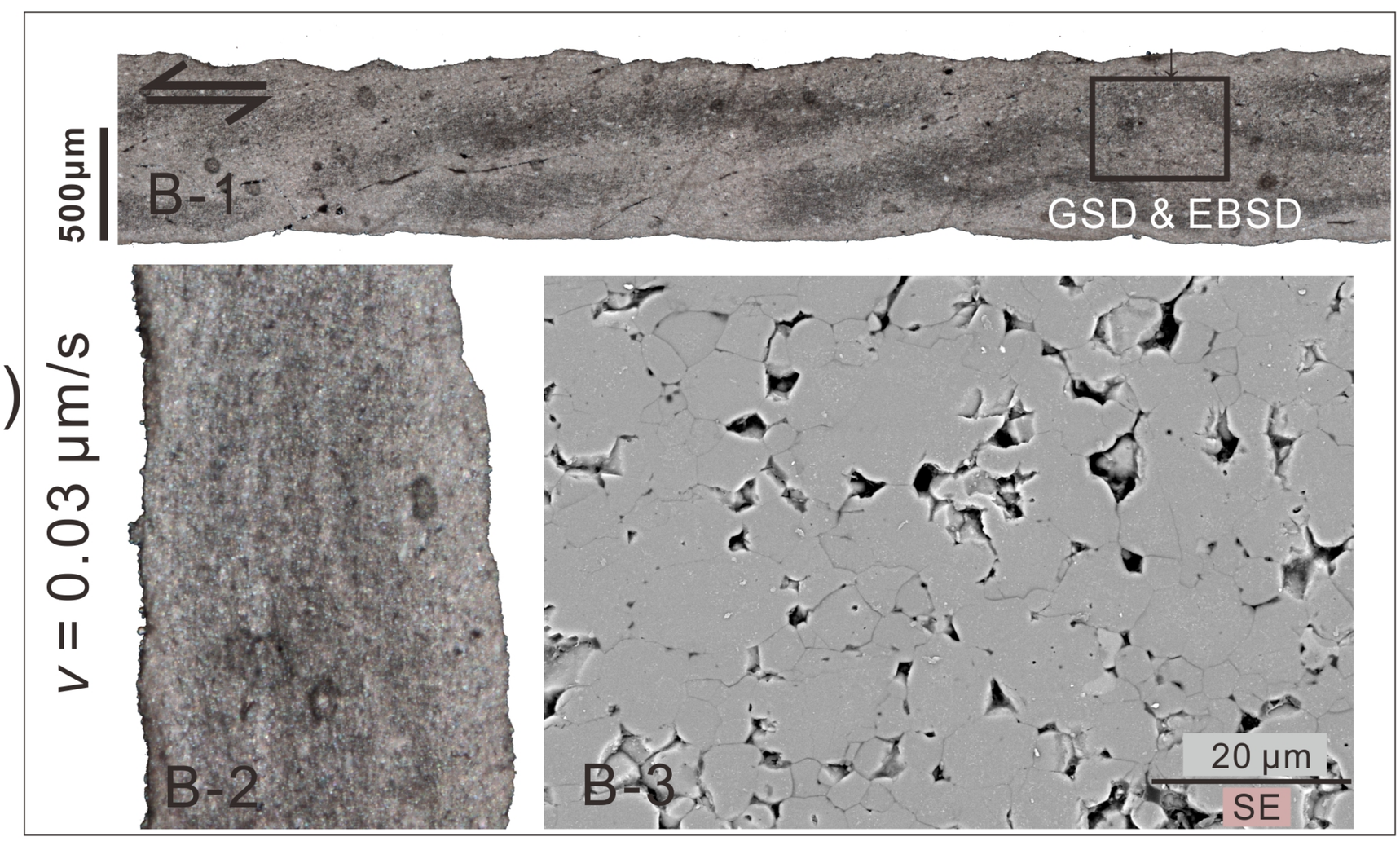
500μm
B-1
GSD & EBSD
v = 0.03 μm/s
B-2
B-3
20 μm
SE

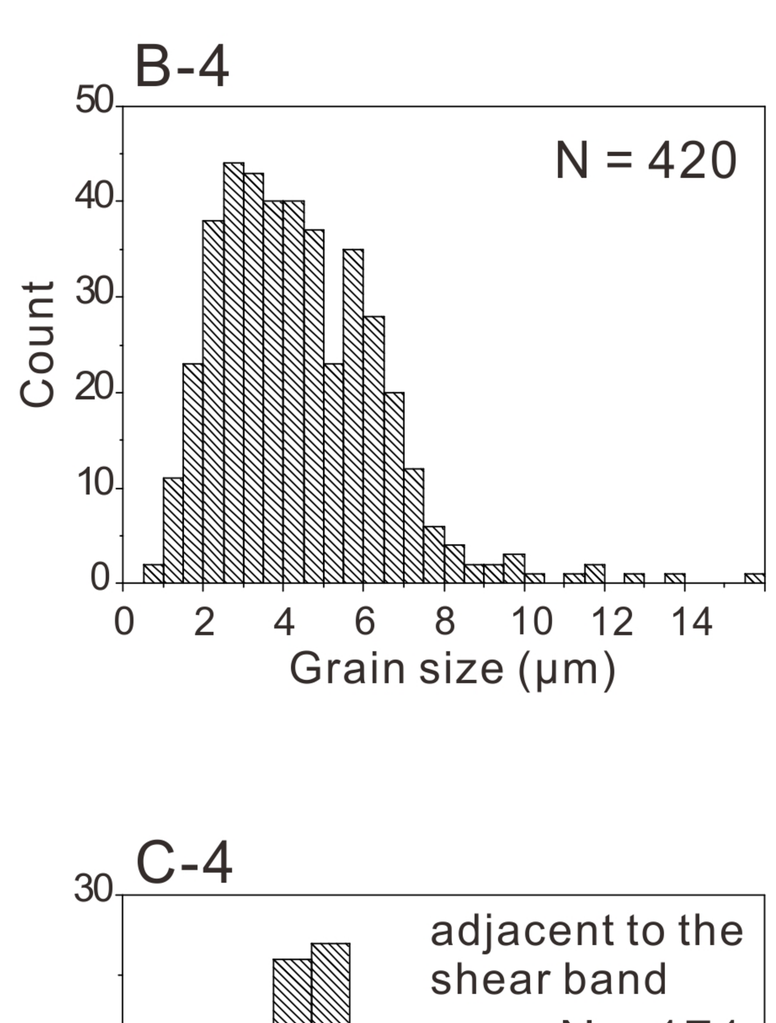
B-4
N = 420
Count
Grain size (μm)

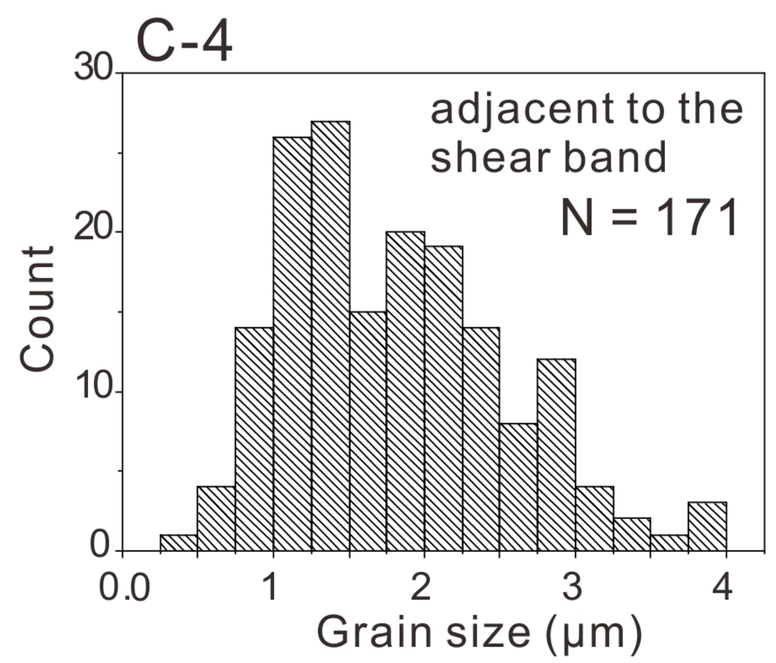
C-4
adjacent to the shear band
N = 171
Count
Grain size (μm)

C)

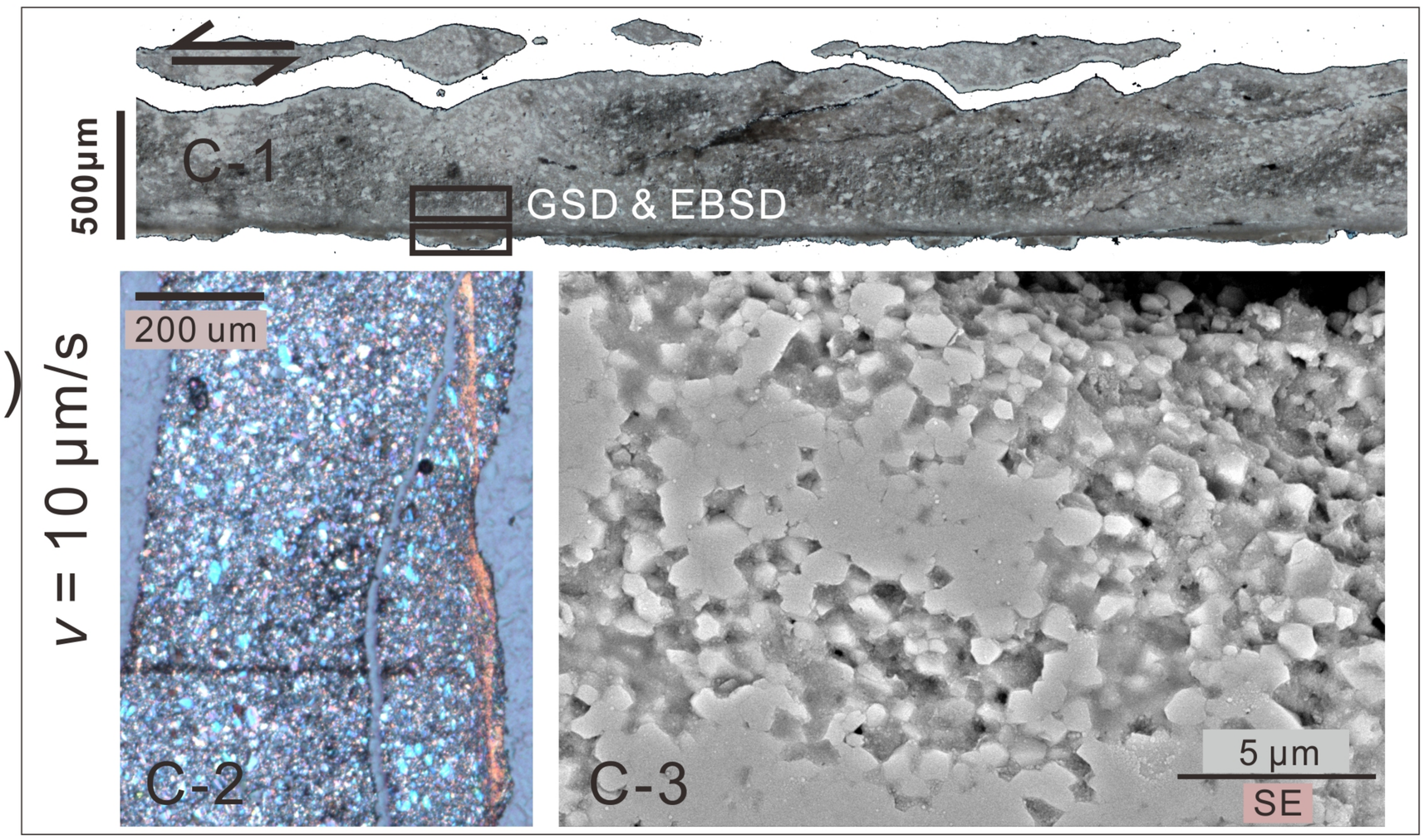
500μm
C-1
GSD & EBSD
v = 10 μm/s
200 um
C-2
C-3
5 μm
SE

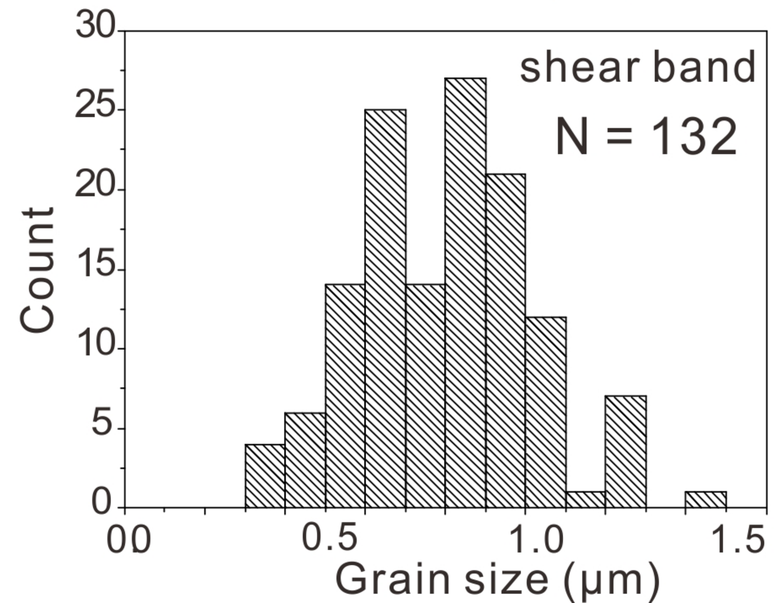
shear band
N = 132
Count
Grain size (μm)

Figure 6.

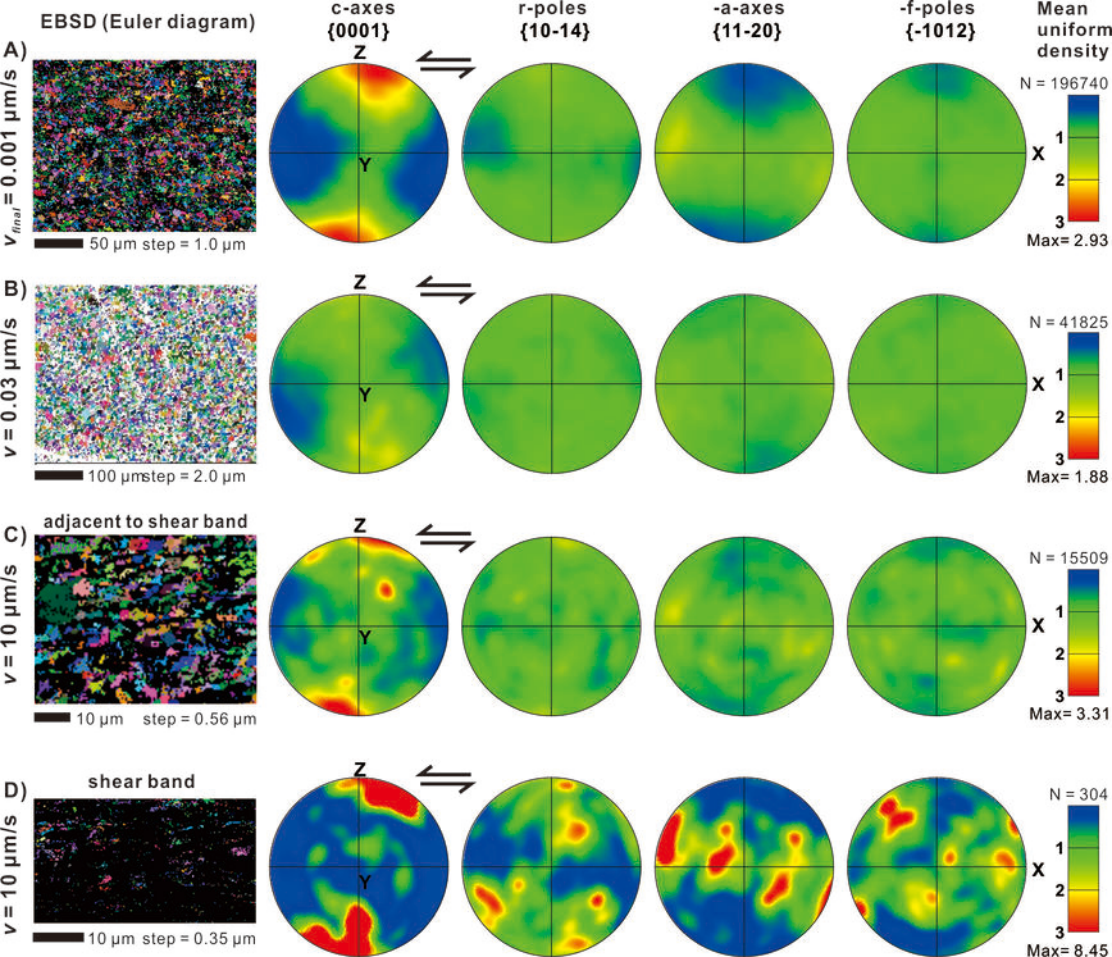
EBSD (Euler diagram)
c-axes {0001}
r-poles {10-14}
-a-axes {11-20}
-f-poles {-1012}
Mean uniform density
A)
v_{final} = 0.001 µm/s
50 µm step = 1.0 µm
N = 196740
Max= 2.93
B)
v = 0.03 µm/s
100 µmstep = 2.0 µm
N = 41825
Max= 1.88
C)
adjacent to shear band
v = 10 µm/s
10 µm step = 0.56 µm
N = 15509
Max= 3.31
D)
shear band
v = 10 µm/s
10 µm step = 0.35 µm
N = 304
Max= 8.45
Z
Y
X
1
2
3

Figure 7.

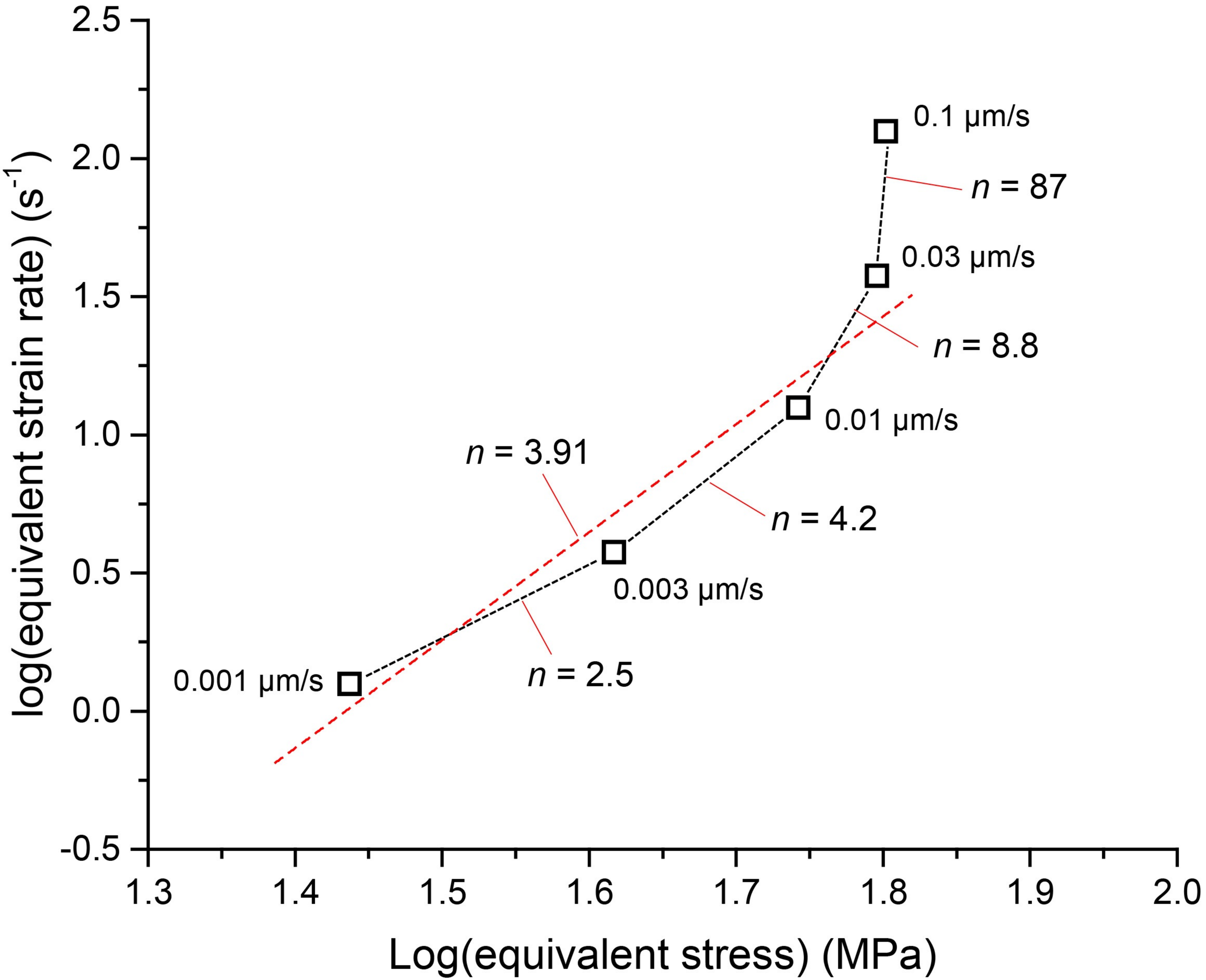
2.5
2.0
1.5
1.0
0.5
0.0
-0.5
log(equivalent strain rate) (s-1)
1.3
1.4
1.5
1.6
1.7
1.8
1.9
2.0
Log(equivalent stress) (MPa)
0.1 μm/s
n = 87
0.03 μm/s
n = 8.8
0.01 μm/s
n = 3.91
n = 4.2
0.003 μm/s
0.001 μm/s
n = 2.5

Figure 8.

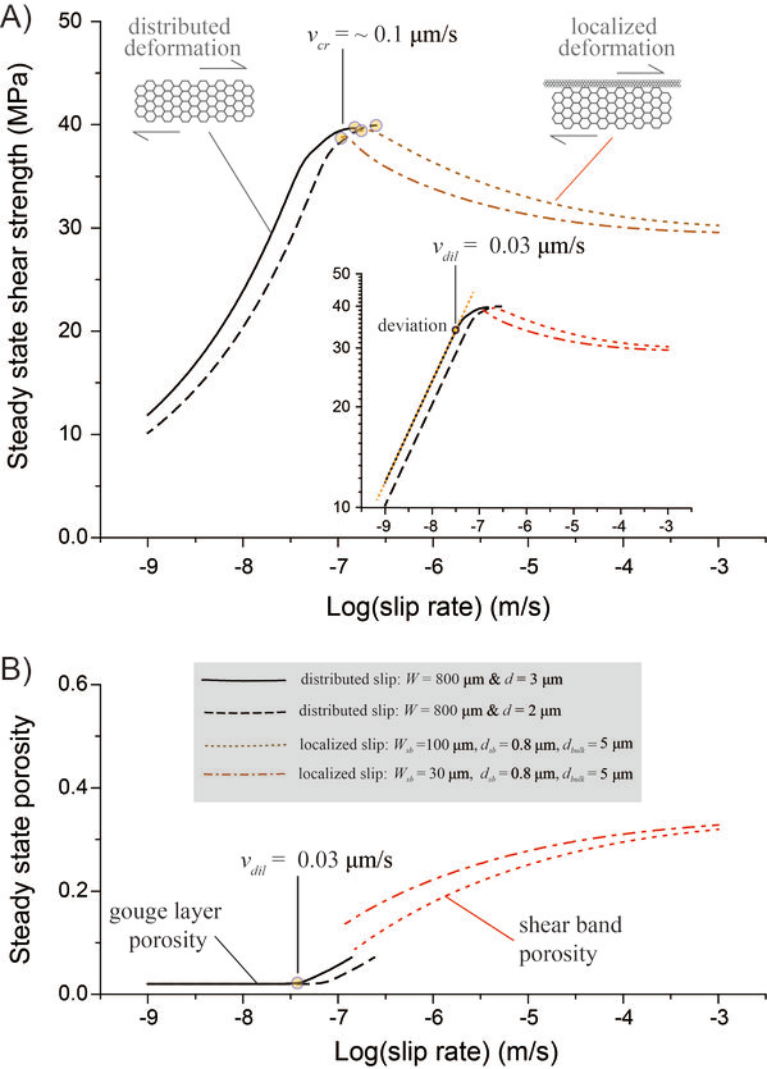
A)
distributed deformation
v_{cr} = ~ 0.1 μm/s
localized deformation
v_{dil} = 0.03 μm/s
deviation
Steady state shear strength (MPa)
Log(slip rate) (m/s)
B)
distributed slip: W = 800 μm & d = 3 μm
distributed slip: W = 800 μm & d = 2 μm
localized slip: W_{sb} =100 μm, d_{sb} = 0.8 μm, d_{bulk} = 5 μm
localized slip: W_{sb} = 30 μm, d_{sb} = 0.8 μm, d_{bulk} = 5 μm
v_{dil} = 0.03 μm/s
gouge layer porosity
shear band porosity
Steady state porosity
Log(slip rate) (m/s)

Figure 9.

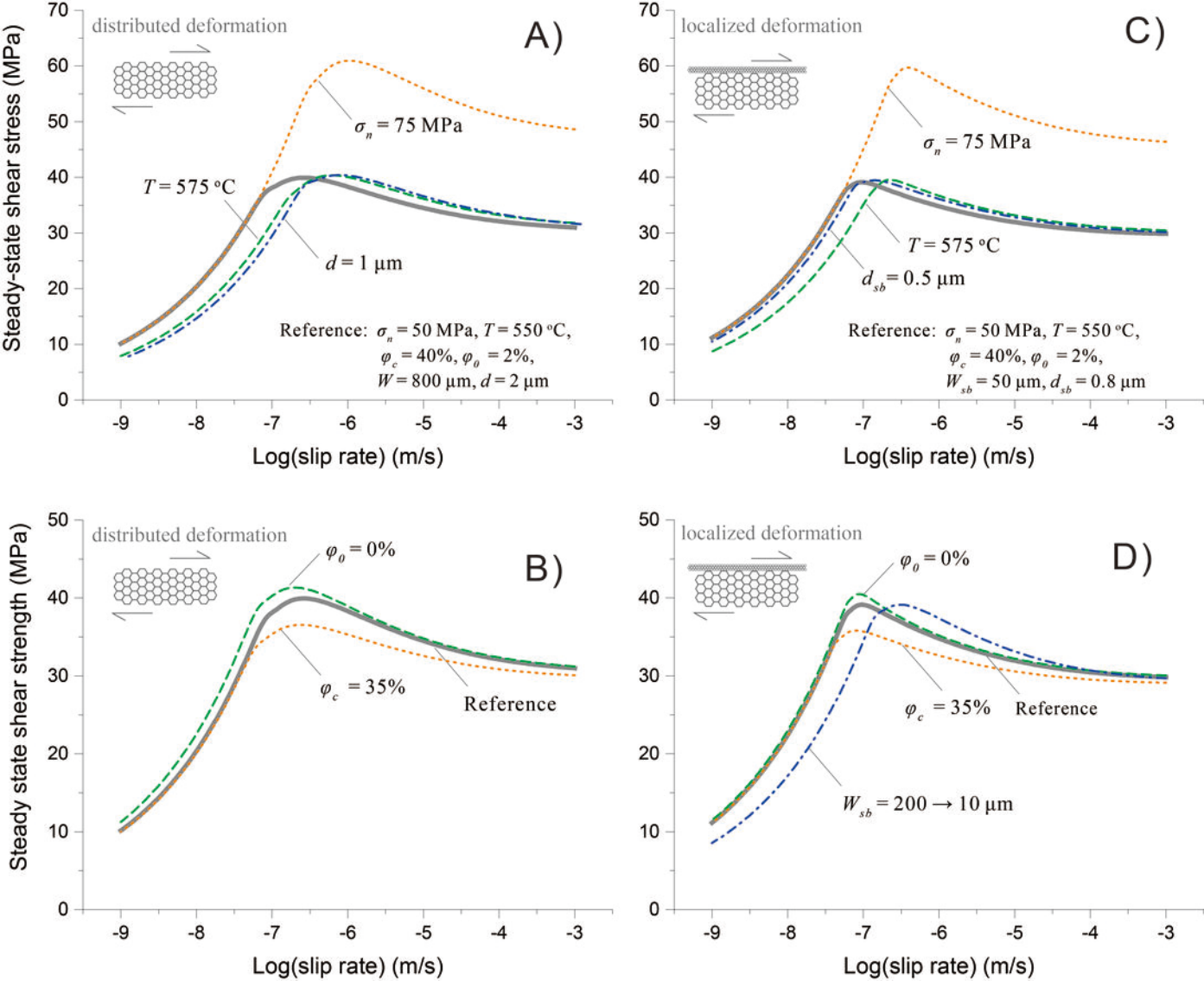
distributed deformation
A)
σ_n = 75 MPa
T = 575 °C
d = 1 μm
Reference: σ_n = 50 MPa, T = 550 °C,
φ_c = 40%, φ_0 = 2%,
W = 800 μm, d = 2 μm
Steady-state shear stress (MPa)
Log(slip rate) (m/s)
localized deformation
C)
σ_n = 75 MPa
T = 575 °C
d_{sb} = 0.5 μm
Reference: σ_n = 50 MPa, T = 550 °C,
φ_c = 40%, φ_0 = 2%,
W_{sb} = 50 μm, d_{sb} = 0.8 μm
Log(slip rate) (m/s)
distributed deformation
B)
φ_0 = 0%
φ_c = 35%
Reference
Steady state shear strength (MPa)
Log(slip rate) (m/s)
localized deformation
D)
φ_0 = 0%
φ_c = 35%
Reference
W_{sb} = 200 → 10 μm
Log(slip rate) (m/s)

Figure 10.

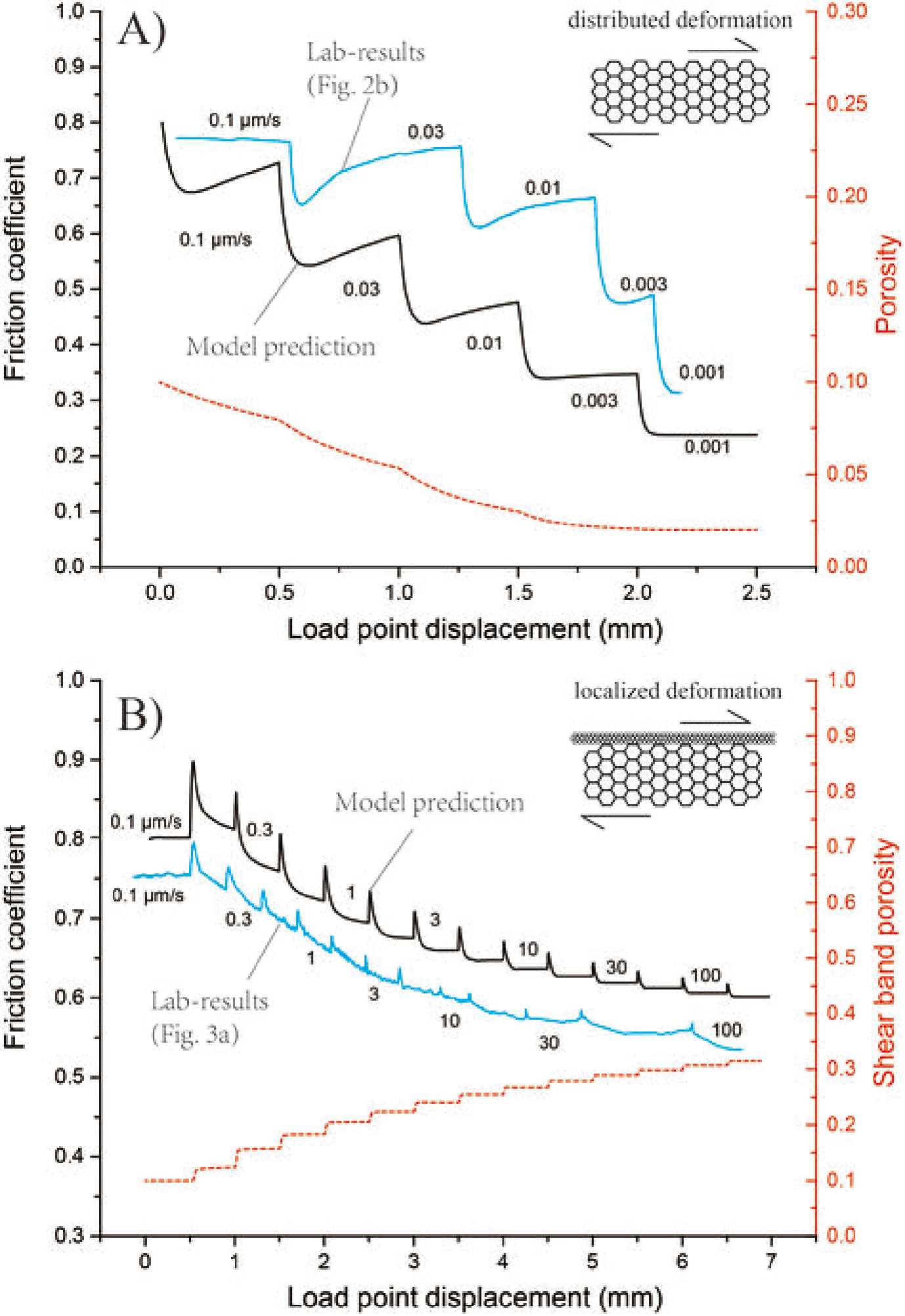
A)
distributed deformation
Lab-results
(Fig. 2b)
0.1 µm/s
0.03
0.01
0.003
0.001
0.1 µm/s
0.03
0.01
0.003
0.001
Model prediction
Friction coefficient
Porosity
Load point displacement (mm)
B)
localized deformation
Model prediction
0.1 µm/s
0.3
1
3
10
30
100
0.1 µm/s
0.3
1
3
10
30
100
Lab-results
(Fig. 3a)
Friction coefficient
Shear band porosity
Load point displacement (mm)

Figure 11.

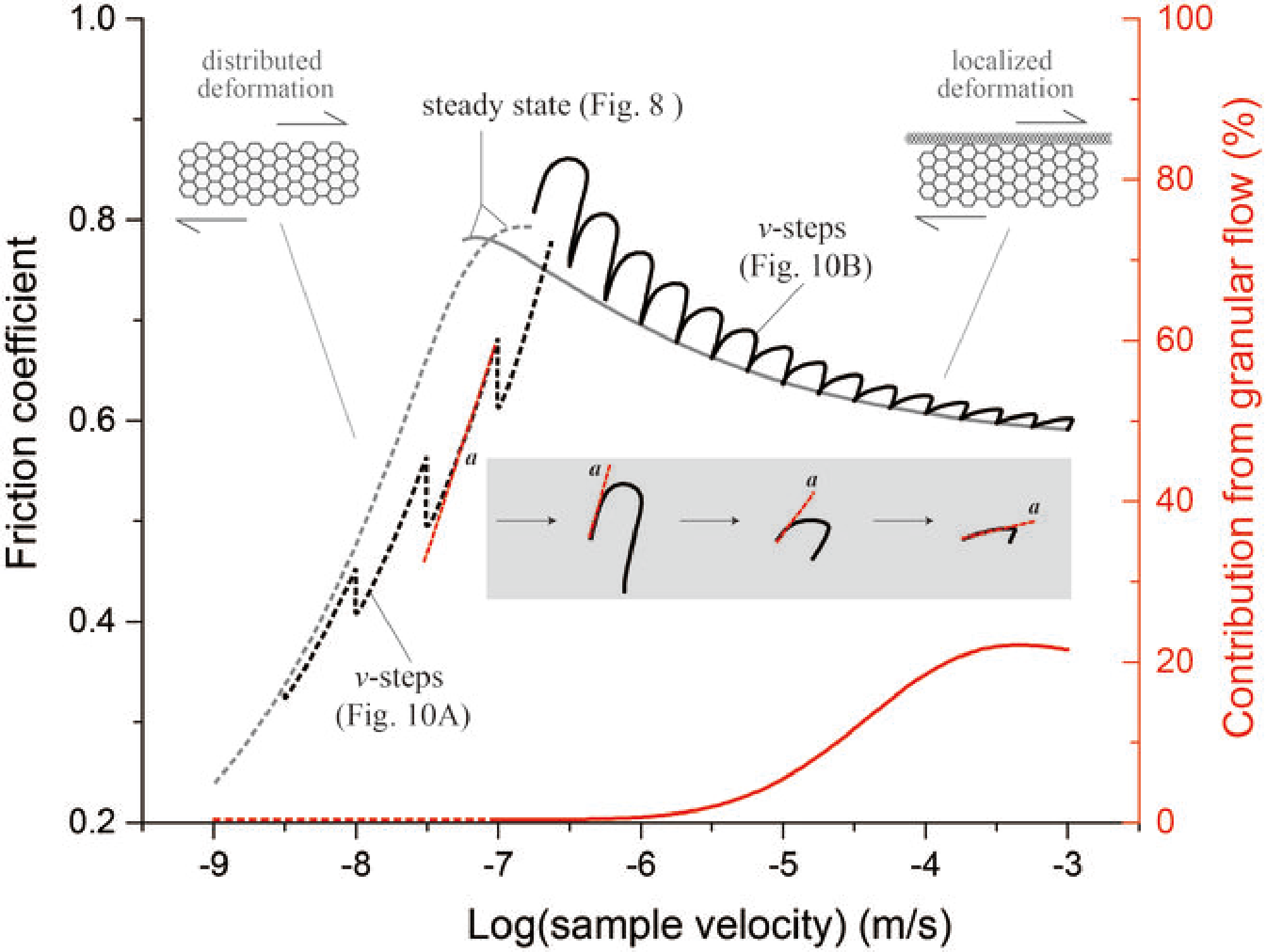
distributed deformation
steady state (Fig. 8)
localized deformation
v-steps (Fig. 10B)
v-steps (Fig. 10A)
a
a
a
a
Friction coefficient
1.0
0.8
0.6
0.4
0.2
-9
-8
-7
-6
-5
-4
-3
Log(sample velocity) (m/s)
100
80
60
40
20
0
Contribution from granular flow (%)

Figure 12.

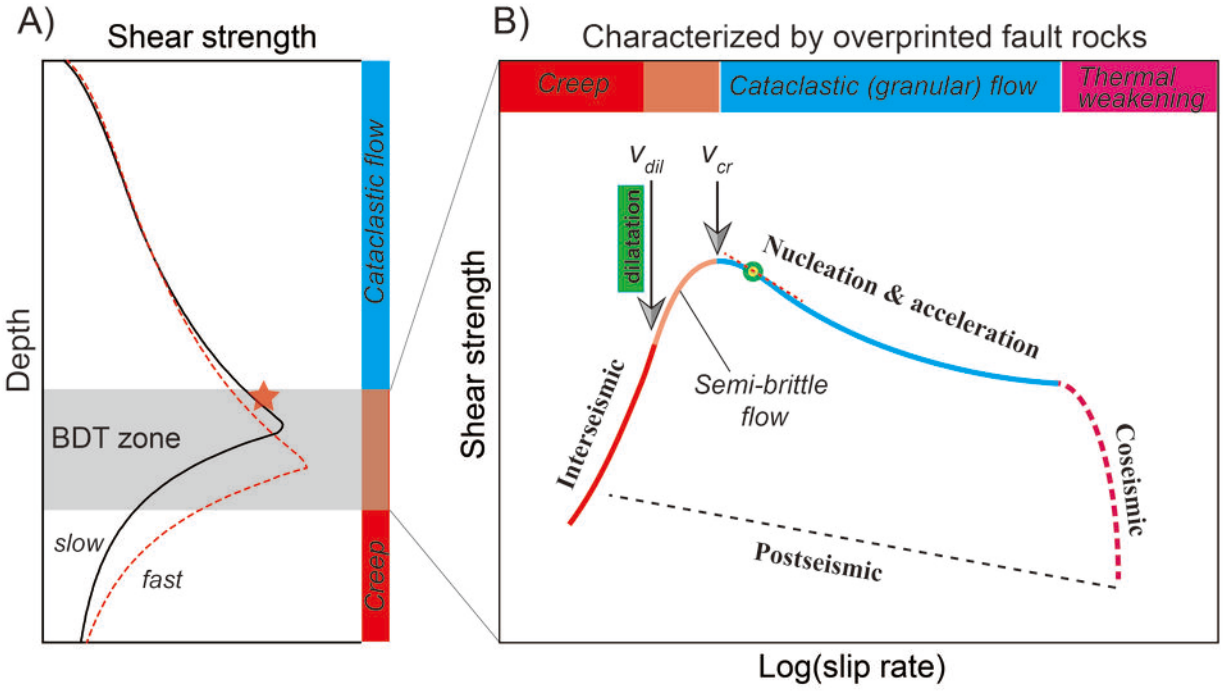
A)
Shear strength
Depth
BDT zone
slow
fast
Cataclastic flow
Creep
B)
Characterized by overprinted fault rocks
Creep
Cataclastic (granular) flow
Thermal weakening
V_{dil}
V_{cr}
dilatation
Nucleation & acceleration
Semi-brittle flow
Interseismic
Coseismic
Postseismic
Shear strength
Log(slip rate)